

# Role of the low-frequency deformation field on the explosive growth of extratropical cyclones at the jet exit.

## Part II: baroclinic critical region

G. Rivière\* and A. Joly

Centre National de Recherches Météorologiques, Météo-France, Toulouse, France

*November 24, 2004*

*Submitted*

---

\*Corresponding author: Geophysical Fluid Dynamics Laboratory, Princeton University, Forrestal Campus, P.O. Box 308, Princeton, NJ 08542, USA; E-mail: [griviere@princeton.edu](mailto:griviere@princeton.edu)

## Abstract

The aim of the paper is to better understand the role of the large-scale deformation field on the strong development of midlatitude cyclones in the jet-exit region. The same methodology as in part I is employed here to treat reanalysis data, i.e the atmospheric flow is decomposed into a high and low-frequency part and new low-frequency diagnostics derived from quasigeostrophic theoretical results are used. The study focuses here on a 4DVAR reanalysis data over north Atlantic at the end of December 1999 when two exceptional wind storms 'Lothar' (24-26 December 1999) and 'Martin' (26-28 December 1999) developed in the jet-exit region and led to huge damages in western Europe.

The explosive growth stages of the two Christmas wind storms in the jet-exit region are characterized by strong peaks of the baroclinic generation and conversion rates far downstream of the baroclinicity maximum. This is shown to result from a transient favourable baroclinic configuration between upper-level disturbances and surface cyclones. The original aspect of this study is to provide a rationale for the location and occurrence of this favourable baroclinic structure in terms of the constraints imposed by the large-scale circulation. In the upper and lower levels, high-frequency disturbances are shown to be trapped by the deformation field of the corresponding low-frequency jet and more precisely by the quantity  $\sigma_m^2 - \zeta_m^2$ , where  $\sigma_m$  is the low-frequency deformation magnitude and  $\zeta_m$  is the low-frequency relative vorticity. The convergence of the two jets associated with that of the two regions  $\sigma_m^2 - \zeta_m^2$  computed in the lower and upper-levels defines a region called baroclinic critical region where high-frequency disturbances may strongly interact baroclinically.

The comparison between the two studies in part I and part II underlines that two zonal jets may have distinguishable but subtle structure differences in their horizontal inhomogeneities that may cause very different behaviours in the life cycles of midlatitude cyclones, especially in terms of their location.

# 1 Introduction

At the end of December 1999, western Europe was devastated by two extreme wind storms, called “Lothar” and “Martin” (hereafter respectively denoted T1 and T2), that caused huge material damages and many human victims. As highlighted by Ulbrich et al. (2001), these two storms developed within a strong zonal jet having a very high baroclinicity. During their explosive growth stage, both cyclones crossed the upper-level large-scale jet from the anticyclonic shear side to the cyclonic one in its diffluent part, i.e far downstream of the environmental baroclinicity maximum. Despite these common features, the two developing storms seem to have large differences. Wernli et al. (2001) (referred hereafter to as W01) emphasized diabatic processes involved in “Lothar” development and noted that there is no apparent, clear PV anomalies at the tropopause level interacting with the cyclone prior to crossing the jet. Conversely, Hello and Arbogast (2004) mentioned the baroclinic interaction between a well defined upper-level precursor and the surface cyclone “Martin” according to the classical type-B development (Petterssen and Smebye, 1971).

The present part of the work aims at understanding the role played by the environmental deformation on the explosive growth of the two storms. Note at this point that the jet of December 1999 is not only exceptional by its large values of baroclinicity but also by its strong horizontal gradients, especially on the northern side. The questions naturally addressed here, following the results of part I, are: do the two extreme storms of December 1999 have the same growth mechanism as IOP17 of FASTEX while moving into the left jet-exit region ? Can we interpret the location of the explosive phase of growth in terms of a constraint given by the large-scale deformation field ?

The same methodology as in part I is applied. It is based on a series of theoretical results from Rivière et al. (2003,2004) (hereafter referred to as RHK03 and RHK04) on perturbation growth in spatially and temporally complex quasigeostrophic flows. The use of the results of RHK03 and RHK04 as well as the decomposition of the atmospheric flow into a high and

low-frequency part allow us to establish some useful low-frequency diagnostics to interpret the role of the large-scale deformation field on the path and growth of the high-frequency synoptic eddies. Furthermore, local energetics are used as the basic framework to confirm quantitatively our ideas.

Section 2 briefly recalls the theory on the deformation field action of RHK03 and RHK04. The methodology is summarized in section 3 since it has been developed in more details in part I. Section 4 deals with reanalysis results from the period from 23 to 28 of December 1999; the spatial structure of the low-frequency deformation field during this period is presented as well as its relation with the high-frequency disturbances location, and a detailed description of the explosive phase of growth of “Lothar” and “Martin” with an energy budget analysis is also made in this section. Section 5 provides a discussion of the results.

## 2 Theory

All the following analytical results are detailed in RHK03, RHK04 and in part I of the present work: they are only briefly recalled in the present section. The following perturbation equations are obtained by decomposing the actual flow into a reference component (which satisfies momentum equations and whose quantities are denoted with overbars) and a perturbation (whose quantities are denoted with primes) and by linearizing momentum equations. In quasigeostrophic flows, the barotropic generation rate that allows a perturbation to extract barotropically kinetic energy from the reference flow can be written as the scalar product  $\mathbf{E}_g \cdot \mathbf{D}_g$  (Mak and Cai, 1989) where

$$\mathbf{E}_g \equiv \left( \frac{1}{2}(v_g'^2 - u_g'^2), -u_g'v_g' \right), \quad (1)$$

$$\mathbf{D}_g \equiv \left( \frac{\partial \bar{u}_g}{\partial x} - \frac{\partial \bar{v}_g}{\partial y}, \frac{\partial \bar{v}_g}{\partial x} + \frac{\partial \bar{u}_g}{\partial y} \right), \quad (2)$$

where  $u_g$  and  $v_g$  are the two components of the geostrophic velocity.  $\mathbf{E}_g$  depends on perturbation anisotropy and  $\mathbf{D}_g$  is the deformation vector whose components are the stretching

and shearing terms of the reference flow. If  $\mathbf{E}_g \cdot \mathbf{D}_g > 0$  (resp  $\mathbf{E}_g \cdot \mathbf{D}_g < 0$ ), the perturbation extracts energy from (loses energy to) the reference flow. By noting that the modulus of the  $\mathbf{E}_g$  vector is the perturbation kinetic energy ( $|\mathbf{E}_g| = K'_{eg} \equiv (v_g'^2 + u_g'^2)/2$ ), and by defining  $\bar{\sigma} \equiv |\mathbf{D}_g|$  the modulus of the  $\mathbf{D}_g$  vector and  $\xi'$  the angle such as  $(\widehat{\mathbf{D}_g, \mathbf{E}_g}) \equiv \pi/2 + \xi'$ , the barotropic conversion rate can be reexpressed as

$$\mathbf{E}_g \cdot \mathbf{D}_g = K'_{eg} \bar{\sigma} \sin \xi'. \quad (3)$$

The sign of  $\mathbf{E}_g \cdot \mathbf{D}_g$  depends directly on the angle  $\xi'$ , whose time evolution equation can be derived (see part I). The equation determining the time evolution of  $\xi'$  has two fixed points which depend solely on the reference flow properties

$$\xi' = \xi_{\pm}^r \equiv \pm \arccos(-r), \quad (4)$$

where  $r = (\bar{\zeta} + 2\frac{\bar{D}_g\bar{\phi}}{Dt})/\bar{\sigma}$ ,  $\bar{\zeta}$  is the basic flow relative vorticity, and  $-2\frac{\bar{D}_g\bar{\phi}}{Dt}$  is the rotation rate of the deformation vector  $\mathbf{D}_g$  along a Lagrangian path as  $(\widehat{\mathbf{Ox}, \mathbf{D}_g}) \equiv \pi/2 - 2\bar{\phi}$  is the angle between the  $x$ -axis and the  $\mathbf{D}_g$  vector. The fixed point  $\xi_-^r$  implies kinetic energy extraction from the reference flow to the perturbation and is an unstable orientation whereas the other ( $\xi_+^r$ ) leads to loss of perturbation kinetic energy and is a stable orientation. If  $\xi'$  is equal to one of the fixed points, following eq.(3), the exponential barotropic kinetic energy generation rate is equal to

$$\frac{\mathbf{E}_g \cdot \mathbf{D}_g}{K'_{eg}}(\xi' = \xi_{\pm}^r) = \pm \sqrt{\bar{\sigma}^2 - \left(\bar{\zeta} + 2\frac{\bar{D}_g\bar{\phi}}{Dt}\right)^2}, \quad (5)$$

and depends only on the reference flow properties.

### 3 Methodology

Previous results are applied by replacing the decomposition into a reference flow and a perturbation by the decomposition into a low-frequency part (denoted with subscript m) and a high-frequency one (denoted with primes). As in part I, the low-frequency is defined

as the time-mean over 8 days centered on the current date and the high-frequency field is the subtraction of the total field from the low-frequency one.

### 3.1 Application of the theory

As in the first part of the paper, the rotation rate of the low-frequency deformation vector, can be neglected because of the weak curvature of the jet. The preferred orientations defined in Eq.(4) can be therefore expressed as

$$\xi_{\pm}^r \simeq \pm \arccos\left(-\frac{\zeta_m}{\sigma_m}\right). \quad (6)$$

Following the expression (5) of the exponential barotropic generation rate, we define also the following quantity (called effective deformation) as in part I

$$\Delta_m \equiv \sigma_m^2 - \zeta_m^2, \quad (7)$$

where  $\zeta_m$  and  $\sigma_m$  are respectively the relative vorticity and the deformation vector modulus of the low-frequency flow.

The angle of the contraction (resp. dilatation) axis with respect to the  $x$ -axis is equal to  $0.5(-\pi/2 - 2\phi_m)$  (resp.  $0.5(\pi/2 - 2\phi_m)$ ). The fixed points  $\xi_-^r$  and  $\xi_+^r$  define two new axes whose angle with respect to the  $x$ -axis are respectively  $0.5(-\arccos(-\frac{\zeta_m}{\sigma_m}) - 2\bar{\phi})$  and  $0.5(\arccos(-\frac{\zeta_m}{\sigma_m}) - 2\bar{\phi})$ . Note that they differ respectively from the contraction and dilatation axes in the general case where the low-frequency relative vorticity  $\zeta_m$  is non zero.  $\zeta_m$  acts on the orientation of the perturbation as well as the stretching and shearing terms and indirectly modifies the barotropic generation term. Positive values of  $\Delta_m$  correspond to regions where synoptic eddies can be strongly stretched due to the action of the deformation field, and in these regions, barotropic processes can be very important. The complementary regions, where the relative vorticity dominates the deformation magnitude, no fixed points exist, it means that the action of the rotation of the relative vorticity is so strong that the perturbation

cannot be stretched along a given orientation. In other words, in the last regions, the shape of the perturbation is almost isotropic and barotropic processes are therefore quite weak.

### 3.2 Energy conversion rates and interpretation

The barotropic generation rate and the baroclinic conversion and generation rates appearing in the high-frequency kinetic and potential energy equations are defined in the present section.

The barotropic generation rate has been already introduced in the previous section for quasigeostrophic flows but the general form used for studying reanalysis data in spherical coordinates is the scalar product  $\mathbf{E} \cdot \mathbf{D}_m$  where

$$\mathbf{E} \equiv \left( \frac{1}{2}(v'^2 - u'^2), -u'v' \right), \quad (8)$$

$$\mathbf{D}_m \equiv \left( \frac{\partial u_m}{\partial x} - \frac{\partial v_m}{\partial y} - \frac{v_m \tan \varphi}{a}, \frac{\partial v_m}{\partial x} + \frac{\partial u_m}{\partial y} + \frac{u_m \tan \varphi}{a} \right). \quad (9)$$

$u$  and  $v$  are the two components of the horizontal velocity,  $\varphi$  is latitude,  $a$  is the radius of the earth,  $\partial/\partial x \equiv (a \cos \varphi)^{-1} \partial/\partial \lambda$  and  $\partial/\partial y \equiv a^{-1} \partial/\partial \varphi$  are the horizontal derivatives and  $\lambda$  is longitude.

The baroclinic conversion rate from eddy potential energy to eddy kinetic energy is equal to  $-\mathcal{R} \theta' \omega'$ , where  $\mathcal{R} \equiv \frac{R}{p} \left( \frac{p}{p_0} \right)^{\frac{C_v}{C_p}}$ ,  $\theta$  is the potential temperature,  $\omega$  is the vertical velocity in pressure coordinates,  $R$  is the gas constant,  $p_0$  is a reference pressure,  $C_v$  and  $C_p$  are the specific heats of the air, at constant volume and pressure.

The baroclinic generation term that converts the available potential energy of the mean flow to eddy potential energy can be written as the scalar product  $\mathbf{F} \cdot \mathbf{B}_c$  in the same manner as Cai and Mak (1990) where the two vectors  $\mathbf{F}$  and  $\mathbf{B}_c$  are defined by

$$\mathbf{F} \equiv \frac{1}{\sqrt{S}} \theta' (v', -u'), \quad (10)$$

$$\mathbf{B}_c \equiv \left( \frac{-1}{\sqrt{S}} \frac{\partial \theta_m}{\partial y}, \frac{1}{\sqrt{S}} \frac{\partial \theta_m}{\partial x} \right). \quad (11)$$

A simple way to interpret the baroclinic generation term is to divide it by eddy total energy  $T'_e$ . This leads to the following expression

$$\frac{\mathbf{F} \cdot \mathbf{B}_c}{T'_e} = |\mathbf{B}_c| \cdot \text{conf} = |\mathbf{B}_c| \cdot \frac{|\mathbf{F}|}{T'_e} \cos(\mathbf{F}, \mathbf{B}_c), \quad (12)$$

where

$$\frac{|\mathbf{F}|}{T'_e} = \frac{\sqrt{\frac{1}{S}\theta'^2(u'^2 + v'^2)}}{\frac{1}{2}(u'^2 + v'^2) + \frac{1}{2S}\theta'^2}, \quad (13)$$

and where  $\cos(\mathbf{F}, \mathbf{B}_c)$  is the cosine of the two vectors  $\mathbf{F}$  and  $\mathbf{B}_c$ . The term  $\mathbf{F} \cdot \mathbf{B}_c$  is called the exponential baroclinic generation rate as it appears in the equation governing the total energy exponential growth rate. It is the product of the baroclinicity  $|\mathbf{B}_c|$  with a term, hereafter called configuration term and denoted *conf*, corresponding to the eddy spatial configuration relative to the baroclinicity vector orientation. The configuration term is itself the product of two terms,  $|\mathbf{F}|/T'_e$  and  $\cos(\mathbf{F}, \mathbf{B}_c)$ , which are related to two well-known different notions of instantaneous optimal baroclinic configuration.  $\cos(\mathbf{F}, \mathbf{B}_c)$  is maximum when the two vectors  $\mathbf{F}$  and  $\mathbf{B}_c$  are colinear; if the two vectors are not colinear, it means that the upper-level disturbance does not align with the surface cyclone along the baroclinicity vector and the whole high-frequency perturbation does not extract optimally the available potential energy of the mean flow. The second term  $|\mathbf{F}|/T'_e$  is related to the tilt with height of the high-frequency perturbation isolines. Indeed, following eq.(13),  $|\mathbf{F}|/T'_e$  is maximum when  $u'^2 + v'^2 = \frac{1}{S}\theta'^2$ , i.e when kinetic energy equals to potential energy; this equality is not satisfied if the high-frequency isolines are strongly tilted, as  $u'^2 + v'^2 << \frac{1}{S}\theta'^2$  in this case, or if they are almost vertical, as it implies  $u'^2 + v'^2 >> \frac{1}{S}\theta'^2$ . The equality  $u'^2 + v'^2 = \frac{1}{S}\theta'^2$  defines therefore a specific vertical slope for the high-frequency geopotential isolines which can be found by approximating  $u', v'$  with the horizontal derivatives of the geopotential and  $\theta'$  with the vertical one. This given slope of the high-frequency perturbation isolines which maximizes  $|\mathbf{F}|/T'_e$  can be related to a notion of distance by considering the interaction between a surface cyclone and an upper disturbance.  $\cos(\mathbf{F}, \mathbf{B}_c) = 1$  is satisfied if the surface



cyclone is aligned with the upper disturbance along the baroclinicity vector and if the former is located ahead of the latter but the condition  $|\mathbf{F}|/T'_e = 1$  is fulfilled if the surface cyclone is at a given distance of the upper disturbance in order to get the slope of the perturbation isolines close to the optimum. The second notion of optimal configuration is equivalent to the phase quadrature condition between the upper-level wave and lower-level one discussed for example in Hoskins et al. (1985). Let us finally emphasize that the optimality of the baroclinic configurations discussed previously is considered only in the instantaneous sense of the term and no notion of time duration intervenes.

## 4 Reanalysis results from the period 23-28 of December 1999

The data is provided by the four-dimensional variational (4DVAR) reanalysis dataset of the period going from December 23 to December 28 1999 at 00, 06, 12, 18 UTC and forecast datasets of the same period but at 03, 09, 15 and 21 UTC. The use of datasets every 3 hour is useful here to analyze the development of the two windstorms since their spatial structure and growth change very rapidly with time. The 4DVAR reanalysis dataset is obtained from the same codes as those of the 4DVAR reanalysis of FASTEX used in part I (see Desroziers et al., 2003), namely Météo-France operational 4DVAR ARPEGE system. It has the noticeable advantage over other datasets to be the only model to consistently forecast the trajectory of the first storm over a wide set of forecast ranges.

### 4.1 Structure of the low-frequency deformation field and its relation with high-frequency disturbances

The low-frequency deformation magnitude  $\sigma_m$  at 12 UTC 26 December is very large north of the jet core (see Fig.1.a) and has a second maximum north of the jet-exit region over

northern France. The maxima of the effective deformation  $\Delta_m$  (see Fig.1.b) are strongly related to those of the deformation magnitude as  $\Delta_m$  has also two well defined regions of large positive values, one north of the jet core and another over western Europe. But in the jet-entrance region,  $\Delta_m$  is positive on the anticyclonic side of the jet by contrast with the two previously mentioned regions and there exists a point of separation around 57W, 43N between two regions of positive values of  $\Delta_m$  respectively located on the southern and northern sides of the jet. This point cannot be viewed in the deformation magnitude field as the latter is not large on the anticyclonic side of the jet in the jet entrance. This point is similar to the barotropic critical region discussed in the first part of the paper, and it will be shown to play an important role in the dynamics of the high-frequency disturbances in the upper-troposphere. However, it has to be noticed that this point is located slightly upstream of the jet core whereas in the jet of February 1997 a barotropic critical region exists in the jet-exit region. There is no barotropic critical region for the jet of December 1999 from its core to its exit because east of longitude 50W, regions of positive  $\Delta_m$  are all located on the northern side only (see Fig.1.b). It is in particular interesting to note that in regions where this jet reaches its maximum speed, between 50W and 20W, the effective deformation  $\Delta_m$  is positive on the northern side exactly where  $\sigma_m$  is the largest. This is to be contrasted with the middle of the jet of February 1997 where the region of positive  $\Delta_m$  is located on the southern side (region numbered 2 in Fig.2.(b) of part I) whereas  $\sigma_m$  is stronger on the northern side again. In other words, despite the fact that in both jets, the deformation magnitude  $\sigma_m$  and the relative vorticity  $\zeta_m$  are the strongest on the northern side of the jet core, the relative amplitude between the two quantities can be very different in such a way that in one case  $\Delta_m$  is positive on the southern side and in the other, on the northern one. This emphasizes the new information given by the effective deformation  $\Delta_m$  on jets asymmetries.

In Fig.2, the high-frequency relative vorticity density at 350 hPa between December 23

and December 28 is computed in the same manner as in part I (see appendix of part I for more details) and consists in counting at each grid point during this period the number of times that  $\zeta'$  is greater than a given threshold.  $10^{-4}\text{s}^{-1}$  is a reasonable threshold for the upper-tropospheric high-frequency relative vorticity to detect the most significant disturbances as it can be seen from instantaneous fields in Figs. 6-9. Different threshold conditions have been tested above this value leading to the same results as in Fig.2 where the threshold condition used is  $\zeta' > 1.25 \cdot 10^{-4}\text{s}^{-1}$ . The density is compared to the low-frequency wind modulus (Fig.2.a) as well as to the low-frequency effective deformation  $\Delta_m$  (Fig.2.b). Following Fig.2.a, the high-frequency disturbances are, to a large extent, located on the anticyclonic side of the jet between  $80^\circ\text{W}$  and  $55^\circ\text{W}$  but between  $55^\circ\text{W}$  and  $45^\circ\text{W}$ , they tend to move to the north of the jet, and from  $45^\circ\text{W}$  until  $20^\circ\text{E}$ , i.e from the jet core to the jet exit, their structures are entirely located on the cyclonic side of the jet. Fig.2.b shows clearly that the density of the high-frequency disturbances is almost everywhere included in regions where  $\Delta_m$  is positive. In particular, the point of separation around  $57^\circ\text{W}$ ,  $43^\circ\text{N}$  between two regions of positive values of  $\Delta_m$  corresponds to the region where the high-frequency disturbances tend to cross the jet from its anticyclonic side to its cyclonic one. Furthermore, from the jet core to its exit, all the disturbances are located on the cyclonic side of the jet as well as the positive values of  $\Delta_m$ .

The same comparison as in Fig.2 is done in Fig.3 but at a low level (850 hPa). In Fig.3.a, a narrow low-level jet appears clearly between  $50^\circ\text{W}$  and  $20^\circ\text{W}$ , it extends towards  $0^\circ\text{W}$  but it seems influenced by the orography of Iberian peninsula between  $20^\circ\text{W}$  and  $0^\circ\text{W}$ . The low-frequency effective deformation  $\Delta_m$  is also perturbed by orography between  $20^\circ\text{W}$  and  $0^\circ\text{W}$  but has a well defined region of positive values between  $50^\circ\text{W}$  and  $20^\circ\text{W}$  north of the low-level jet. The high-frequency relative vorticity density at 850 hPa between December 23 and December 28 is shown in Fig.3.b, and is essentially composed of the high-frequency relative vorticity associated with the signal of the two storms. This high-frequency activity

is clearly superimposed upon the region of positive values of  $\Delta_m$  between 50°W and 20°W on the north side of the jet. Notice also that the high-frequency disturbances tend to propagate along an axis oriented SW-NE which is precisely the axis of the low-frequency low-level jet and of the low-frequency diagnostic  $\Delta_m$ .

Figs.4.a-b represent the vertical cross sections at the longitude 36°W at two different dates 06 UTC 25 December and 18 UTC 26 December. These vertical cross sections underline the baroclinic structure of the low-frequency jet and of the effective deformation  $\Delta_m$  around the jet core and their relation to the high-frequency disturbances. The high-frequency relative vorticity is represented with solid black contours and the structures related to T1 and T2 are respectively in the lower side of Fig.4.a and Fig.4.b. The boundary  $\Delta_m = 0$  which corresponds to the line of maximum low-frequency velocity clearly exhibits the baroclinic structure of the low-frequency jet with a northward tilt with height. Most of the high-frequency relative vorticity contours are included in regions of positive  $\Delta_m$  and the upper-level disturbances are significantly more located north of their low-level counterparts. Fig.4 confirms the statistical results described previously but from an instantaneous point of view and underlines the impact of the baroclinic structure of the low-frequency jet on the latitudinal shift of the upper-level disturbances related to the surface cyclones.

The last figures have shown that the low-frequency large-scale circulation during the end of December 1999 has a complex tridimensional structure characterized by a low-level jet located far in the south of the upper-level jet over the Atlantic; at longitude 40W, the distance separating the lower from the upper level jets is very important (almost 10° in latitude as shown in Fig.5.a) and the separation distance is then decreasing farther eastward where the wind speed of the jets is also decreasing. Note that this property can be deduced from semigeostrophic theory, the stronger the wind speed of the jet, the larger the distance between the two jets. Figs.5.a-b is a sketch explaining how this separation between the two jets and their related effective deformation fields acts in such a way that baroclinic interaction cannot

be strong in the jet-core region. In this sketch, the assumption is that there is a positive baroclinic interaction between a surface cyclone and an upper-level disturbance during its trajectory along the jet, and the aim is to show that the interaction cannot be strong around the jet core because of the constraints imposed by the deformation field and despite the presence of the baroclinicity maximum, whereas this interaction can be optimized in the jet-exit region. Regions of positive  $\Delta_m$  in the upper and lower-levels are respectively represented in a simplified manner by the solid and dashed gray arrows in Figs.5.a-b; regions of positive  $\Delta_m$  at 350 hPa form approximately a zonally oriented corridor (Fig.2.b) while the same quantity at 850 hPa forms a corridor whose orientation is SW-NE (Fig.3.b). Fig.5.a depicts the case where the two disturbances at the upper and lower-levels (solid and dashed black circles) are located around the jet-core region; as they are forced to be in regions of positive  $\Delta_m$ , their structures are centered along the solid and dashed gray arrows respectively. From this configuration, we deduce the orientation of the  $\mathbf{F}$  vector shown in Fig.5.a (black arrow) and denoted  $\mathbf{F}_1$ . The low-frequency jet is zonal and the baroclinicity vector  $\mathbf{B}_c$  is almost zonal as shown by the field of gray arrows in Fig.5.c.  $\mathbf{F}_1$  has a NW-SE orientation, the angle between  $\mathbf{F}_1$  and  $\mathbf{B}_c$  is acute and leads to a positive scalar product  $\mathbf{F}_1 \cdot \mathbf{B}_c > 0$  but this angle is quite large and corresponds therefore to a non optimal baroclinic interaction (see Fig.5.c). Moreover, the two high-frequency disturbances are quite far to each other, which suggests that the high-frequency isolines are strongly tilted, and the two notions of optimal instantaneous configuration described in section 3.3 and more specifically in eq.(12) are therefore not satisfied. When the two disturbances have reached the jet-exit region (Fig.5.b), the composite structure they make up together is aligned with the baroclinicity vector. They can be sufficiently close to each other to also have the right tilt with height for the high-frequency isolines while satisfying the constraint of location in a region of positive  $\Delta_m$  as shown in Fig.5.b. In this case,  $\mathbf{F}_2$  is indeed colinear to the baroclinicity vector  $\mathbf{B}_c$  as shown in the right side of Fig.5.c. The baroclinic configuration is significantly more optimal

in the configuration related to  $\mathbf{F}_2$  in the jet-exit region than that related to  $\mathbf{F}_1$  in the jet-core region. Although the magnitude of the baroclinicity vector  $|\mathbf{B}_c|$  is decreasing in the jet-exit region (compare the amplitude of the  $\mathbf{B}_c$  vectors in the jet-exit and jet-core regions in Fig.5.c), a favourable baroclinic configuration in the jet-exit region can compensate for this to the extent that the baroclinic interaction in the jet-exit region is stronger than in the jet-core one. To conclude, as high-frequency disturbances in the upper and lower-levels are both forced to evolve along the corridors determined by regions of positive  $\Delta_m$ , a strong interaction is possible between the two types of high-frequency disturbances only in the area where the two regions of positive  $\Delta_m$  in the upper and lower levels converge; this area is hereafter called the baroclinic critical region. In the following sections, the aim is to confirm the idea that the explosive growth of the wind storms in the jet-exit region can be explained by a strong transient baroclinic interaction due to a favourable baroclinic configuration which itself can be explained by the constraints imposed by the  $\Delta_m$  field on the high-frequency disturbances trajectories.

## 4.2 Description of the explosive growth of T1 and T2 at the jet exit

Figs.6, 7, 8 and 9 present the evolution of the two storms; their associated relative vorticity at 850 hPa is shown with dashed black contours; the high-frequency relative vorticity in the upper-troposphere at 350 hPa is represented by solid black contours. Between 00 UTC 25 December and 12 UTC 26 December (Figs.6.a-c, Figs.7.a-c and Fig.8.a), the first storm T1 evolves from central Atlantic to western Europe while the evolution of the 2nd storm T2 is visible from 18 UTC 25 December to 18 UTC 27 December (see Figs.7.b-c, Figs.8.a-c and Figs.9.a-c).

From these figures, the trajectories of the two storms is parallel to an axis oriented SW-NE. This axis is linked to the low-level jet axis and its spatial inhomogeneities, as discussed

in the previous section, is simply represented by the dashed gray arrow in Fig.5 and by the dashed gray line in Figs.6, 7, 8 and 9. During their evolution along this axis, i.e in a region characterized by positive values of  $\Delta_m$ , the two storms are stretched by the deformation field. In the appendix, the elongation axis of each storm is compared to the dilatation axis and the stable axis deduced from the theory described in section 2. It is shown that the two storms are more stretched along the stable axis than the dilatation axis which underlines the consistency of our approach.

Let us now discuss the interaction of T1 with the high-frequency disturbances in the upper-troposphere. The configuration in Fig.6.a-c between the surface cyclone T1 and the upper-level disturbance is quite similar to the schematic picture shown in Fig.5.a, i.e the surface cyclone T1 interacts baroclinically with the closest upper-level disturbance which is located northwest of its structure. The reality of this baroclinic interaction is confirmed by the energy budget analysis shown below but it remains weak as the two high-frequency disturbances are quite far from each other and there is no alignment of the high-frequency disturbances along the baroclinicity vector. However, when the low-level cyclone is already at the same latitude as the upper disturbances (Fig.7.b) at 00 UTC 26 December, the situation between the high-frequency disturbances at the upper and lower-levels is comparable with that shown in Fig.5.b and a strong baroclinic interaction occurs at this moment. A quantitative study is performed in the next sections to verify this qualitative description and especially in the comments describing Fig.13.

The trajectory of T2 and the location of its explosive phase of growth are quite similar to those of T1 but a large difference has to be noticed between the two storms; T2 interacts with a well defined pre-existing upper-level disturbance during its whole life cycle (see from Fig.7.c to Fig.9.c) whereas although T1 interacts with upper-level disturbances during its evolution, it does not interact with the same one. A discussion related to the study of W01 is provided in section 5, especially concerning the appearance or the pre-existence of the

upper-level disturbance interacting with T1 during its explosive growth stage.

Consider now the interaction between T2 and the well defined pre-existing upper-level disturbance. At 00 UTC 26 December and 06 UTC 26 December (Figs.7.a-b), the upper-level anomaly is located south of the jet in a region of positive  $\Delta_m$  and has a clear anticyclonic elongation (a SW-NE tilt). Its structure is still quite far from the surface cyclone T2 and the interaction is not strong. From 12 UTC 26 December to 00 UTC 27 December (Figs.8.a-c), the upper-level disturbance crosses the jet, its structure changes rapidly as it begins to be stretched zonally. Let us emphasize that this rapid crossing of the jet occurs about the point of separation previously defined between two regions of positive  $\Delta_m$  and located at 57W, 43N. An explanation of this crossing will be given in the next paragraph. The result at 00 UTC 27 December is that the upper-level disturbance is almost located north of the upper-level jet and the spatial configuration between the upper disturbance and the surface cyclone is quite similar to that of Fig.5.a, i.e baroclinic interaction exists but is not yet optimal. The optimality of this interaction occurs at 12 UTC 27 December and 18 UTC 27 December, when the upper disturbance and the surface cyclone are close to each other and aligns with the baroclinicity vector (similar to the sketch in Fig.5.b). The two criteria for favourable baroclinic configuration are satisfied at this moment. Although the scenario of the explosive growth of the two storms is not completely the same, the area where the explosive growth occurs is similar and is due to the constraints imposed by the large-scale deformation and its three-dimensional structure.

### 4.3 Energy budgets

Fig.10 shows how the upper-level disturbance interacting with T2 is forced to cross the jet from the anticyclonic side to the cyclonic one between 00 UTC 26 December and 00 UTC 27 December. At 00 UTC 26 December (Fig.10.a), the upper-level disturbance is entirely on the anticyclonic side of the jet and is strongly stretched along the dilatation axes. In



this case, the dilatation axis and the stable axis of section 2 are almost parallel. Most of the perturbation isolines are along the dilatation axes and a large barotropic sink occurs leading to a decrease of the amplitude of the upper-level disturbance (compare the number of contours of the high-frequency relative vorticity in Figs.10.a, b and c). But because of the orthogonality of the dilatation axes between those located on the cyclonic side of the jet and those on the anticyclonic one, the high-frequency isolines are perpendicular to the dilatation axes on the cyclonic side and parallel on the anticyclonic one leading to barotropic increase on the former side and decrease on the latter (see Figs.10.a and b). At 00 UTC 27 December (Fig.10.c), most part of the high-frequency disturbance is already on the cyclonic side and still increases barotropically; the part being on the anticyclonic side disappears due to barotropic decrease. This barotropic mechanism is similar to that shown in the first part of the work for the surface cyclone of IOP17 of FASTEX and explains why the high-frequency structure disappears on the anticyclonic side and appears on the other side. Let us finally emphasize that the location of such a mechanism can be known apriori by looking at the  $\Delta_m$  field; it tends indeed to occur around points of separation between two regions of positive  $\Delta_m$  located respectively in both sides of the jet.

Figs.11.a-b represent the time evolution of volume integrals of different quantities, the baroclinic generation rate, the low-frequency baroclinicity, the eddy total energy and the exponential generation rate. These volume integrals are made exactly in the same manner as in part I, i.e each quantity is first vertically averaged between two isobars (here between 900 hPa and 250 hPa) and then horizontally averaged by considering only grid points inside a circle whose center is the barycenter around T1 (resp. T2) of the absolute values of the vertically averaged baroclinic generation rate. The baroclinic generation rate has a well defined peak for both storms, at 03 UTC 26 December for T1 (Fig.11.a) and at 15 UTC 27 December for T2 (Fig.11.b). This peak is not at all due to a peak of baroclinicity as the peak of the baroclinic generation rate (thick solid line with diamonds in Fig.11.a-b) occurs when

baroclinicity is decreasing (dash-dotted line in Fig.11.a-b). This result is not astonishing as the two storms strongly intensify in the jet-exit region, and thus far away from the baroclinicity maximum. But the exponential baroclinic generation rate (dashed line in Fig.11.a-b) composed of the multiplication of the baroclinicity by the configuration term is maximum exactly at the same time as the baroclinic generation rate. The evolution of the baroclinic generation rate is therefore strongly dependent on the baroclinic configuration of the high-frequency disturbances related to the baroclinicity vector. Such a peak in the exponential baroclinic generation rate shows also that the growth of the two storms is stronger than an exponential, and can be characterized by a “superexponential” growth.

In Fig.12, the time evolution of the high-frequency kinetic energy maximum computed at low levels (maximum of the vertical average between 500 hPa and 900 hPa) around T1 (Fig.12.a) and T2 (Fig.12.b) are compared to those of the barotropic generation rate  $\mathbf{E.D_m}$  and the baroclinic conversion rate  $-\mathcal{R}\theta'\omega'$  at the same levels around T1 (Fig.12.c) and T2 (Fig.12.d). The maximum of kinetic energy at low levels is analyzed instead of an average, in order to understand better the peak of velocity of these wind storms responsible for huge damages in western Europe. From Fig.12.a and Fig.12.b, it appears that the explosive growth of T1 and T2 occur respectively from 18 UTC 25 December to 0900 UTC 26 December and from 06 UTC 27 December to 18 UTC 27 December. During these two periods of strong kinetic energy growth, the baroclinic conversion rate from eddy potential energy to eddy kinetic energy is very strong and has two well defined peaks at 03 UTC 26 December and at 15 UTC 27 December which correspond also to two peaks of the baroclinic generation rate (see Figs.11.a-b). These two peaks of the baroclinic conversion rates slightly precede the peaks of eddy kinetic energy maximum and take place when the slope of the eddy kinetic energy curve is the strongest. The barotropic generation rate by contrast is significantly smaller than the baroclinic conversion rate and does not play a role in the explosive growth of the two storms. The fact that barotropic processes are negligible in the jet-exit region was

expected as no barotropic critical region (in the sense of part I) was present from the jet core to the jet exit, and in this region, at each level, high-frequency disturbances move along the northern side of the low-frequency jet. The barotropic generation rate only has a large signal in the upper-troposphere between 00 UTC 26 December and 00 UTC 27 December when the upper-level disturbance associated with T2 crosses the jet as shown in Fig.10. This signal is not present however in the curve of Fig.12.b as the latter pertains to low levels only (between 500 hPa and 900 hPa). Concerning the redistribution terms of energy (not shown here), the term related to the horizontal ageostrophic geopotential fluxes is negative in average around each storm during their explosive growth of kinetic energy and act therefore to disperse energy away from the region of growth as for the IOP17 of FASTEX (part I).

Figs.13 and 14 describe more precisely the baroclinic configuration of respectively T1 and T2 according to their position along the jet and will be intercompared with the schematic picture of Fig.5. At 12 UTC 25 December, the vector  $\mathbf{F}$  computed at the point where  $\mathbf{F} \cdot \mathbf{B}_c$  is maximum around T1 is oriented NW-SE (see Fig.13.a) as it was predicted in Fig.5 which confirms that there is baroclinic interaction with the upper-level high-frequency structure located northwest of the surface cyclone. This interaction has been already suggested by looking at the high-frequency relative vorticity contours of Fig.6.c and is here confirmed by the orientation of  $\mathbf{F}$  and by the geopotential isolines which present at 350hPa a local minimum northwest of T1 around the point (45W,50N) (see the left side of Fig.13.a). As  $\mathbf{B}_c$  is almost zonal,  $\mathbf{F}$  and  $\mathbf{B}_c$  are not colinear,  $\cos(\mathbf{F}, \mathbf{B}_c)$  is not close to 1, a positive baroclinic interaction is present but not optimal in terms of the alignment along the baroclinicity vector. Fig.13.c is a vertical cross section of the high-frequency geopotential isolines at the same date and plotted along the  $\mathbf{F}$  vector, and not along  $\mathbf{B}_c$  as it is done usually, as  $\mathbf{F}$  represents the main direction of the baroclinic interaction. On this cross section, one can see T1, the upper-level structure upstream of it, and a clear northwestward tilt with height of the high-frequency geopotential isolines confirming the presence of a classical baroclinic interaction.

Furthermore, as the two-levels high-frequency disturbances are quite far from each other, the geopotential isolines going from the lower to the upper troposphere are strongly tilted. Consider now the baroclinic generation rate  $\mathbf{F} \cdot \mathbf{B}_c$  plotted in Fig.13.c with shaded contours; there exists two distinct regions with large values of  $|\mathbf{F} \cdot \mathbf{B}_c|$  but with opposite signs. The region with positive values is close to T1 and is related to the westward tilt with height discussed previously but there is also a region with negative values in the middle troposphere, located below and east of the upper-level structure. These negative values are also visible in the vertical average of  $\mathbf{F} \cdot \mathbf{B}_c$  in Fig.13.a around the point (40W,50N). Such a region was not present in Fig.5.a, i.e in our schematic picture of baroclinic interaction in the jet-core region but this sink of baroclinic conversion seems to be also due to the global interaction between T1 and the upper-level structure and more specifically due to the fact that T1 is quite far from the upper-level structure at this date. As it will be shown, this sink indeed disappears as T1 is moving closer to the upper-level structure in the jet-exit region.

At 03 UTC 26 December (right column in Fig.13), T1 is already in the jet-exit region and the magnitude of the baroclinicity vector  $|\mathbf{B}_c|$  has decreased as expected (see the decrease of the magnitude of the gray arrow in Fig.13.b). The angle between  $\mathbf{F}$  and  $\mathbf{B}_c$  in Fig.13.b is almost the same as in Fig.13.a which suggests an interaction of the surface cyclone again with an upper-level structure located northwest of it. This is confirmed by noting that the upper-level high-frequency geopotential has a local minimum centered over Ireland around the point (10W,53N) while the minimum of geopotential in the low levels is around (2W,49N). The main difference between the two baroclinic interactions of Figs.13.a and b is not characterized by a change in the alignment along  $\mathbf{B}_c$  but rather by a decrease of the relative distance between the upper-level high-frequency structure and the surface cyclone. The convergence of the two-level high-frequency disturbances in the jet-exit region has been already seen in Figs.6 and 7 with relative vorticity isolines and is here shown with geopotential contours. In particular, the vertical cross sections of Figs.13.c-d show that the upper-level disturbance is

closer to T1 at 03 UTC 26 December than at 12 UTC 25 December. The first consequence is that the geopotential isolines are less strongly tilted in Fig.13.d than in Fig.13.c; the vector  $\mathbf{F}/T'_e$  has a larger magnitude in Fig.13.b than in Fig.13.a but only slightly (20% larger) which confirms that the tilt in Fig.13.d is effectively more optimal than in Fig.13.c. A second consequence of this move of T1 toward high-frequency upper-level structures seems to be also the disappearance of the baroclinic sink at 03 UTC 26 December. Both, the disappearance of the baroclinic sink and the slight improvement of the tilt are responsible for the peak of the average of the configuration term in Fig.11.a.

Fig.14 is equivalent to Fig.13 but for cyclone T2. The upper-level disturbance is located northwest of T2 at 00 UTC 27 December (see Fig.14.a), as it can be seen also from the relative vorticity contours of Fig.8.c, and  $\mathbf{F}$  and  $\mathbf{B}_c$  are not colinear as expected from the schematic picture of Fig.5. The baroclinic interaction is shown in Fig.14.c with a clear northwestward tilt with height. By contrast with T1, we remark that the geopotential isolines are less strongly tilted at this moment because the upper-level disturbance, which is located north of the upper-level jet as expected but very close to the jet-core, is closer to T2. There is no presence of a large baroclinic sink; just a very small negative peak is visible in Fig.14.a around (25W,50N). AT 15 UTC 27 December, there is a clear alignment of  $\mathbf{F}$  with the baroclinicity vector  $\mathbf{B}_c$ , explaining the peak of the configuration term shown in Fig.11.b and the maximum of  $\mathbf{F} \cdot \mathbf{B}_c$  is almost 3 times larger at 15 UTC 27 December than at 00 UTC.

To conclude on the comparison between Figs.13-14 and the schematic picture of Fig.5, Fig.13 strongly suggests that T1 interacts baroclinically with a perturbation in the upper-troposphere even in the beginning of its life cycle with a clear northwestward tilt with height of the geopotential isolines as it was expected from Fig.5 in the jet-core region. Then, T1 converges toward the upper-level structures in the jet-exit region as it was shown in Fig.5 but an unexpected result is that the improvement of the baroclinic configuration term in the jet-exit region is due essentially to the disappearance of a region of baroclinic sink. Fig.14

shows also that, in the jet-exit region, T2, as T1, forms a baroclinic interaction oriented along the NW-SE direction with the upper disturbance. However, by contrast with T1, the evolution of the baroclinic configuration of T2 is closer to the schematic picture of Fig.5 in the sense that there is a clear alignment along the baroclinicity vector in the jet-exit region. Let us finally note another difference between T1 and T2 concerning the amplitude of the baroclinic generation term  $\mathbf{F} \cdot \mathbf{B}_c$ . The maximum of this term for T2 is about 3 times larger than that of T1 (note that the contours are different in Fig.13.b and Fig.14.b) whereas Fig.12 has shown that the maxima of the baroclinic conversion rates are of the same order for T1 and T2. This result possibly suggests that there is another source for the high-frequency eddy potential energy in the case of T1 which could be diabatic terms as W01 has already emphasized.

From this energy budget analysis, it is concluded that a strong transient baroclinic interaction related to a transient optimal baroclinic configuration of the high-frequency disturbances is responsible for the strong intensification of the surface cyclones T1 and T2 in the jet-exit region. Energy redistribution terms as well as barotropic processes do not play an important role in this sudden phenomenon. Diabatic terms play probably a role in this intensification of the phenomenon, especially for T1, but these terms have not been studied as the aim of this study was to explain essentially the location of the phenomenon rather than to understand its real intensity.

## 5 Discussion

Midlatitude cyclones evolving in the northeast Atlantic grow in the jet-exit region and their strongest deepening rates tend to occur downstream of the baroclinicity maximum (see e.g., Fig.15 of Wang and Rogers, 2001). It was in particular the case of the two Christmas wind storms of December 1999. However, such extreme cases occur with the presence of exceptionally strong jets and extremely high baroclinicity (Ulbrich et al., 2001). These results

as well as those of Ayrault and Joly (2000) suggest that large baroclinicity is a necessary condition for the development of strong wind storms but cannot give us any information on the location of their explosive growth stage. The aim of the paper was to show how a modified large-scale deformation acts on the location of synoptic disturbances and force them to interact baroclinically in specific regions.

The 3D view perspective of the large-scale circulation of the end of December 1999 is characterized by the presence of a strong zonal upper-level jet and a SW-NE oriented lower-level jet located in the south of the upper-level one. The two jets are quite far from each other over the Atlantic but “converge” in the eastern Atlantic region, i.e very close to western Europe. Furthermore, the exceptionally strong jet like that of December 1999 leads not only to strong baroclinicity but also to narrow and strong horizontal shears (the maximum of the horizontal deformation magnitude is even 1.3 times larger than that of the baroclinicity). Regions where the effective deformation  $\Delta_m$  is positive are therefore very localized and these regions computed in the upper and lower levels form two narrow corridors north of their respective low-frequency jets that “converge” over the eastern Atlantic region, in an area called in the text baroclinic critical region.

First of all, it has been shown that, at each level, the high-frequency disturbances are trapped in regions where the effective deformation  $\Delta_m$  is positive, underlying the robustness of the results of part I. These constraints of location imposed by  $\Delta_m$  added to the convergence of the two low-frequency jets in the baroclinic critical region shows that the surface cyclone and the upper-disturbances, when both exist, can only strongly baroclinically interact in the baroclinic critical region. Indeed, the argument is the following; suppose that an upper disturbance interacts baroclinically with a surface cyclone in the jet-core region, this baroclinic interaction cannot be optimal for two reasons associated with two well-known notions of favourable baroclinic configuration which cannot be satisfied in this area. First, due to the constraints of location of each disturbance in regions of positive  $\Delta_m$ , the up-

per disturbance cannot align with the surface cyclone along the baroclinicity vector as the perturbation isolines would be tilted northwestwardly with height whereas the tilt must be purely westward to optimally extract energy from the low-frequency flow; second, these perturbation isolines that join the disturbances at the two levels would be much too tilted as the two disturbances are quite far from each other. By contrast, in the jet-exit region, such constraints are not present, the upper-disturbance can be sufficiently close to the surface cyclone to get the appropriate tilt with height and the alignment with the baroclinicity vector can be satisfied too. Let us note that this qualitative argument based on the location of the effective deformation does not suggest that there will be necessarily an upper disturbance each time that will interact with the surface cyclone nor that the deformation field is helping the two disturbances to stay in phase. It does not say either that the two notions of baroclinic configuration will be necessarily optimized in the jet-exit region, but allows to say that if a surface cyclone has an explosive growth in such a weather regime, it can only occur in the baroclinic critical region.

Results of the paper have first shown that T1 and T2 have indeed both undergone a form of baroclinic interaction with high-frequency upper-level structures along the jet. In the jet-core region, where the horizontal deformation field has the strongest magnitude, the baroclinic configuration has exactly the spatial structure as that diagnosed by the constraints imposed by the effective deformation, i.e a non optimal baroclinic configuration characterized by strongly northwestward tilted geopotential isolines. The explosive growth stages of the two Christmas wind storms have been then clearly characterized by well defined peaks of both the baroclinic generation and conversion rates, which are not related to maxima of baroclinicity as the latter quantity is decreasing in the jet-exit region but to an optimization of the baroclinic configuration. This optimization has been diagnosed by the configuration term (defined as the baroclinic generation rate divided by the high-frequency total energy and by the baroclinicity magnitude), which is a proper manner to quantify the combined effect



of the two notions of favourable baroclinic configuration between an upper-level disturbance and a surface cyclone. For T2, there is a clear alignment along the baroclinicity as it is reaching the baroclinic critical region; for T1, there is no improvement of the alignment configuration but its baroclinic configuration is optimized by a more appropriate tilt with height as it is approaching the upper-level high-frequency structure and by the disappearance of a baroclinic sink that seems to result from the move of T1 closer to the upper-level high-frequency structures. The favourable phase between high-frequency disturbances in the upper and lower levels does not last ( $\simeq 12$  hours) and is therefore very far from a normal mode behaviour and in this sense has also to be distinguished from a phase locking configuration as that described in Hoskins et al (1985). The explosive growth phase of these two storms is therefore characterized by a favourable transient baroclinic configuration leading to a “superexponential growth” in the sense that the exponential generation rate is not constant and is strongly increasing during the explosive growth stage.

The exceptionally strong jet like that of December 1999 leads to a strong baroclinicity which is responsible for the intensity of the two explosive storms but also to narrow and strong horizontal gradients and to a significant separation between the upper and lower-levels jets that act on the location of the phenomenon. The results of the present paper go in the same direction as those of James (1987) who has shown in horizontally sheared flows that the barotropic component of the basic flow confines perturbations to be located in specific regions which do not correspond to the most baroclinic part of the basic flow and baroclinic interaction is thus reduced by the presence of the shears. In the same manner, it has been shown here that the confinement of synoptic eddies in regions where  $\Delta_m$  is positive leads to baroclinic interaction far away from the baroclinicity maximum. The advantage of the low-frequency effective deformation  $\Delta_m$  is that it can be applied to any observed low-frequency jet.

Diabatic effects play probably a significant role as well as baroclinic conversion rates in

the intensity of the explosive growth stages of the two storms as it has been discussed by W01 in the development of 'Lothar' or by Mallet et al. (1999) in the case of FASTEX IOP17 studied in part I. The energy budget made in this paper possibly suggests that diabatic effects could be especially important for T1 more than for T2 but as the goal of the present study was to focus more on the location of the phenomenon than its intensity and to explain the former in terms of the dynamical constraints imposed by the large-scale circulation, diabatic effects were not diagnosed more precisely.

Despite the similarity of the two Christmas wind storms in terms of their trajectory and the location of their explosive growth stage, some differences in terms of the scenario exist also which are important in order to discuss the relevance of the Sutcliffe-Petterssen scheme or type-B development (Petterssen and Smebye, 1971). The proposed mechanism to explain the location of the explosive phase of the two storms, as summarized in the previous paragraphs, would imply that there exists preexisting upper-level disturbances interacting with the surface cyclones T1 and T2. It is clear that T2 interacts with the same well defined upper disturbance during its whole life cycle as Hello and Arbogast (2004) have shown and as it has been emphasized in the present paper, but the interaction of T1 with a well defined preexisting upper disturbance seems to be more questionable. W01 have pointed out that, the development of T1 is characterized by a shallow low-level cyclone of moderate intensity which intensifies strongly as it crosses the jet stream axis and no pre-existing well defined upper-level disturbance seems to interact with T1 during its whole life cycle. W01 explains the appearance of an upper-level disturbance during the crossing of the jet by a "bottom-up development" which is an equivalent of Fig.21 of Hoskins et al (1985); the circulation induced by the low-level PV anomaly in the upper-troposphere because of the strong PV gradient around the speed maximum of the jet advects PV southward and creates an upper-level PV anomaly just upstream of the low-level vortex. This last remark seems apriori to contradict our results as we have shown that there exists right north of the jet axis already

a high-frequency upper-level structure before the explosive growth phase of T1 (see for example Fig.7.a) even if it is not a well-defined coherent disturbance. From our high and low frequency decomposition, it is difficult to state that the upper-level disturbance just upstream of the surface cyclone during the explosive growth phase of T1 (Fig.7.c) is the extension of the high-frequency upper-level disturbance located 12 hours before northwest of the surface cyclone (Fig.7.a), or, as the argument of W01 suggests, it is created by the advection of low-frequency PV southward by the circulation induced by the low-level high-frequency PV anomaly. It seems that both the pre-existing high-frequency upper-level structure, and the mechanism described by W01 can be responsible for the presence of the well defined upper-level disturbance in Fig.7.c. Let us emphasize however that our argument on the location of the explosive phase of growth is relevant even if the mechanism depicted by W01 is predominant; indeed, if it was the case, the low-level cyclone would be forced by the effective deformation of the low-frequency jet to follow a SW-NE trajectory and to meet a large upper-level PV gradient only in the jet-exit region and not before and therefore to start an explosive growth only at this moment. To conclude, the upper disturbance that interacts with T2 is clearly visible and supports the classical type-B mechanism whereas the upper-level disturbance associated with T1 is more difficult to follow as a coherent structure evolving in space and time. Following these results and those of part I, it would be surprising to find the development of a cyclone in the eastern Atlantic with a total absence of high-frequency structures before its growth stage. Indeed, this is confirmed by the composite types of development of Ayrault and Joly (2000), that includes a type of cyclone as frequent as bombs but that does not develop although in a strongly baroclinic environment.

The “crossing of the jet” from the warm to the cold-air side in region of diffluence seems to be the preferred place for strong deepening rates of northeastern Atlantic cyclones (Baehr et al., 1999; W01). This result is commonly understood by the analogy with jet streaks theory; as the presence of a jet streak induces surface cyclogenesis in its left-exit region due

to divergence processes created by ageostrophic winds in the upper-level (Uccellini, 1990), in the same manner cyclones will strongly grow in the left-exit region of the large-scale jet stream. It is however difficult to rationalize the dynamical processes involved by doing this parallel between jet streaks and jet streams as the jet streak concerns the total field, i.e has a high and a low-frequency part whereas the jet stream is only a low-frequency quantity. In other words, it is not clear that a low-frequency divergence will strengthen the surface cyclone. The aim of the present paper was to investigate further dynamical processes leading to strong cyclone growth during the “crossing of the jet stream” in its exit region by expliciting scale interaction between disturbances, and their slowly evolving environments. Part I and part II of the present paper exhibit two different realizations of “crossing of the jet”. In part I, it is shown that during the explosive phase of growth, the upper-level disturbance and the surface cyclone respectively cross the upper and lower-level jets from the south to the north and barotropic generation rates play a significant role because of the rapid change of the dilatation axes. This in turn creates or regenerates a baroclinic tilt with height which can take the growth over. In part II, both the upper and lower-level disturbances stay on the northern side of their corresponding jets in the eastern Atlantic. In the latter case, the surface cyclone crosses the upper-level jet, but not the lower-level one and barotropic processes are thus not important during this crossing. A change in the constraints of location imposed by the deformation field along the jet allows the development of a more optimal baroclinic configuration between the upper and lower-level disturbances in the jet-exit region that results in the growth.

Finally, it must be emphasized that the low-frequency effective deformation  $\Delta_m$  has an important predictability potential to help localize regions where wind storms will reach their maximum amplitude. In the jet-exit region,  $\Delta_m$  is useful to anticipate regions where storms will have to go through. For example, large values of  $\Delta_m$  are located north of England for the jet of mid-february 1997 (see Fig.2 of part I), where IOP17 have gained its maximum

amplitude. The same diagnostic for December 1999 is centered over France and Germany (see Figs.6-8) exactly where T1 and T2 have reached their maximum amplitude and have made huge damages. Two zonal jets apparently differing only in terms of their amplitudes have thus subtle but distinguishable structure differences in their horizontal inhomogeneities that may lead to very different behaviours of midlatitude cyclones life cycles and especially in their location. The fact that these differences depend solely on a large-scale, slowly evolving property is of major interest both in terms of understanding cyclogenesis as a scale interaction process and for medium-range prediction of windstorm risk assessment.

## Appendix: Alignment properties

Figs.15.a-b describe the alignment properties of the two surface cyclones associated with T1 and T2 during their evolution north of the low-level jet. The angle of the stable axis with respect to the  $x$ -axis deduced from the theory described in section 3.1 is equal to  $0.5(\arccos(-\zeta_m/\sigma_m) - 2\phi_m)$  while the angle of the dilatation axis with respect to the  $x$ -axis is  $0.5(\pi/2 - 2\phi_m)$ . The two axes are respectively plotted in Figs.15.a-b with gray and black arrows. At 12 UTC 25 December, the surface cyclone associated with T1 is slightly stretched in the zonal direction, exactly in the same direction as the stable axis whereas the dilatation axis has a pronounced NW-SE tilt. At 12 UTC 26 December, the surface cyclone associated with T2 is strongly stretched zonally also and even if the stable axis is not completely zonal, the elongation of T2 is closer to the stable axis than to the dilatation axis. This result shows the consistency of our approach and the non negligible role played by the low-frequency relative vorticity on the orientation of the high-frequency disturbances. Furthermore, it suggests that the name “dilatation axis” is not very appropriate as the structure of the surface cyclone is not dilated along this axis. It is only in very specific cases when the rotational component of the deformation field is zero, as for example in the pure strain case, that it may occur (see RHK03 and RHK04 for a more detailed description on

alignment dynamics).

## References

- Ayrault, F. and Joly, A. 2000. Une nouvelle typologie des dépressions météorologiques: classification des phases de maturation. *C. R. Acad. Sci. Paris, Sciences de la terre et des planètes/ Earth and Planetary Sciences*, **330**, 167-172.
- Baehr, C., Pouponneau, B., Ayrault, F. and Joly, A. 1999. Dynamical characterization of the FASTEX cyclogenesis cases. *Quart. J. Roy. Meteor. Soc.*, **125**, 3469-3494.
- Cai, M. and Mak, M. 1990. On the basic dynamics of regional cyclogenesis. *J. Atmos. Sci.*, **47**, 1417-1442.
- Desroziers, G., Hello, G. and Thepaut, J-N. 2003. Four-dimensional reanalyses of FASTEX. *Quart. J. Roy. Meteor. Soc.*, **129**, 1301-1315.
- Hello, G and Arbogast, P. 2004. Two different methods to correct the initial conditions applied to the storm of 27 December 1999 over southern France. *Meteorolog. Appl.*, **11**, 41-57.
- Hoskins, B. J., McIntyre, M. E. and Robertson, A. W. 1985 On the use and significance of isentropic potential vorticity maps. *Quart. J. Roy. Meteor. Soc.*, **111**, 877-946.
- James, I. N. 1987. Suppression of baroclinic instability in horizontally sheared flows. *J. Atmos. Sci.*, **44**, 3710-3720.
- Mak M. and Cai, M. 1989. Local barotropic instability. *J. Atmos. Sci.*, **46**, 3289-3311.
- Mallet, I., Cammas, J.P., Mascart, P., and Bechtold, P. 1999. Effects of cloud diabatic heating on the early development of the FASTEX IOP17 cyclone. *Quart. J. Roy. Meteor. Soc.*, **125**, 3439-3467.

- Orlanski, I. and Sheldon, J.P. 1995. Stages in the energetics of baroclinic systems. *Tellus*, **47A**, 605-628.
- Petterssen, S. and Smebye, S.J. 1971. On the development of extratropical cyclones. *Quart. J. Roy. Meteor. Soc.*, **97**, 457-482.
- Rivière, G., Hua, B. L. and Klein, P. 2003. Perturbation growth in terms of barotropic alignment properties. *Quart. J. Roy. Meteor. Soc.*, **129**, 2613-2635.
- Rivière, G., Hua, B. L. and Klein, P. 2004. Perturbation growth in terms of baroclinic alignment properties. *Quart. J. Roy. Meteor. Soc.*, **130**, 1655-1673.
- Ulbrich, U., Fink, A. H., Klawe, M. and Pinto, J. G. 2001 Three extreme storms over Europe in December 1999. *Weather*, **56**, 70-80.
- Uccellini, L. W. 1990. Processes contributing to the rapid development of extratropical cyclones. p. 81-105 in *Extratropical cyclones. The Erik Palmén Memorial Volume*. Eds. C. Newton and E. O. Holopainen. American Meteorological Society, Boston.
- Wernli, H., Dirren, S., Liniger, M. A. and Zillig, M. 2002 Dynamical aspects of the life cycle of the winter storm 'Lothar' (24-26 December 1999). *Quart. J. Roy. Meteor. Soc.*, **128**, 405-429.
- Wang, C-C and Rogers, J. C. 2001. A composite study of explosive cyclogenesis in different sectors of the north atlantic. Part I: Cyclone structure and evolution. *Mon. Wea. Rev.*, **129**, 1481-1499.

## List of Figures

- 1 Low-frequency wind speed  $|\mathbf{u}_m|$  at 350 hPa larger than  $40 \text{ m.s}^{-1}$  (dotted shadings and contours, interval  $10 \text{ m.s}^{-1}$ ) with (a) the square of the low-frequency deformation vector modulus  $\sigma_m^2$  larger than  $9.10^{-10} \text{ s}^{-2}$  (shaded contours, interval  $9.10^{-10} \text{ s}^{-2}$ ) and (b) positive values of the low-frequency effective deformation  $\Delta_m$  (shaded contours, interval  $9.10^{-10} \text{ s}^{-2}$ ). . . . . 36
- 2 High-frequency relative vorticity density at 350 hPa during the period 23-28 December 1999 (number of times for which  $\zeta' > 1.25.10^{-4} \text{ s}^{-1}$  at each grid point, hatched shadings) with (a) the low-frequency wind speed  $|\mathbf{u}_m|$  larger than  $40 \text{ m.s}^{-1}$  (dotted shadings and contours, interval  $10 \text{ m.s}^{-1}$ ) and (b) the positive values of the low-frequency effective deformation  $\Delta_m$  (shaded contours, interval  $9.10^{-10} \text{ s}^{-2}$ ). . . . . 37
- 3 Positive values of the low-frequency effective deformation  $\Delta_m$  at 850 hPa (shaded contours, interval  $2.10^{-10} \text{ s}^{-2}$ ) with (a) the low-frequency wind speed  $|\mathbf{u}_m|$  at 850 hPa (dotted shadings and dashed contours for 17,18 and  $19 \text{ m.s}^{-1}$ ) and (b) high-frequency relative vorticity density at 850 hPa during the period 23-28 December 1999 (number of times for which  $\zeta' > 8.10^{-5} \text{ s}^{-1}$  at each grid point, hatched shadings). . . . . 38
- 4 Vertical cross section of the low-frequency wind speed  $|\mathbf{u}_m|$  larger than  $20 \text{ m.s}^{-1}$  (dotted shadings and contours, interval  $10 \text{ m.s}^{-1}$ ), the positive values of  $\Delta_m$  (shaded contours, interval  $3.10^{-10} \text{ s}^{-2}$ ) and the high-frequency relative vorticity larger than  $4.10^{-5} \text{ s}^{-1}$  (thick solid contours, interval  $4.10^{-5} \text{ s}^{-1}$ ) . . . 39



- 5 Schematic picture defining the baroclinic critical region. Low-frequency wind speed  $|\mathbf{u}_m|$  at 350 hPa larger than  $50 \text{ m.s}^{-1}$  (dotted shadings and solid contours, interval  $10 \text{ m.s}^{-1}$ ) and at 850 hPa (dotted shadings and dashed contours for 18 and  $19 \text{ m.s}^{-1}$ ). Positive values of the low-frequency effective deformation  $\Delta_m$  at 350 hPa are shown in shaded contours (interval  $9.10^{-10} \text{ s}^{-2}$ ). The solid and dashed gray arrows represent respectively regions with positive values of  $\Delta_m$  at 350 hPa and 850 hPa from the jet core to its exit which are both located on the northern side of their respective jets. The convergence of these two arrows in the jet-exit region defines the baroclinic critical region. The solid and dashed black circles represent respectively high-frequency disturbances at 350 hPa and 850 hPa evolving (a) in the jet-core region and (b) in the jet-exit region. The black arrows denoted  $\mathbf{F}_1$  and  $\mathbf{F}_2$  are the  $\mathbf{F}$  vector for two different configuration cases shown respectively in (a) and (b). In (c),  $\mathbf{F}_1$  and  $\mathbf{F}_2$  are superposed to the vertically averaged (900-250hPa) baroclinicity vector  $\mathbf{B}_c$  when  $|\mathbf{B}_c| > 2.10^{-5} \text{ s}^{-1}$ . . . . . 40
- 6 Low-frequency wind speed  $|\mathbf{u}_m|$  at 350 hPa larger than  $40 \text{ m.s}^{-1}$  (dotted shadings and contours, interval  $10 \text{ m.s}^{-1}$ ), positive values of the low-frequency effective deformation  $\Delta_m$  at 350 hPa (shaded contours, interval  $9.10^{-10} \text{ s}^{-2}$ ), high-frequency relative vorticity at 350 hPa larger than  $5.10^{-5} \text{ s}^{-1}$  (thick solid contours, interval  $5.10^{-5} \text{ s}^{-1}$ ) and high-frequency relative vorticity at 850 hPa larger than  $4.10^{-5} \text{ s}^{-1}$  (thick dashed contours, interval  $4.10^{-5} \text{ s}^{-1}$ ): (a) 00 UTC 25 Dec, (b) 06 UTC 25 Dec, and (c) 12 UTC 25 Dec. The dashed gray line corresponds to the same axis as the dashed gray arrow of Fig.5, i.e to the thin region of positive  $\Delta_m$  at 850 hPa. . . . . 42
- 7 Same as in Fig.6, but for (a) 18 UTC 25 Dec, (b) 00 UTC 26 Dec and (c) 06 UTC 26 Dec. . . . . 43

8	Same as in Fig.6, but for (a) 12 UTC 26 Dec, (b) 18 UTC 26 Dec and (c) 00 UTC 27 Dec. . . . .	44
9	Same as in Fig.6, but for (a) 06 UTC 27 Dec, (b) 12 UTC 27 Dec and (c) 18 UTC 27 Dec. . . . .	45
10	Barotropic generation rate $\mathbf{E} \cdot \mathbf{D}_m$ at 350 hPa (contour interval is $0.01 \text{ m}^2 \cdot \text{s}^{-3}$ , light shadings with dashed contours and dark shadings with solid contours indicate respectively negative values smaller than $-0.01 \text{ m}^2 \cdot \text{s}^{-3}$ and positive values greater than $0.01 \text{ m}^2 \cdot \text{s}^{-3}$ ), low-frequency wind speed $ \mathbf{u}_m $ at 350 hPa larger than $40 \text{ m} \cdot \text{s}^{-1}$ (dotted shadings), the high-frequency relative vorticity larger than $5 \cdot 10^{-5} \text{ s}^{-1}$ (thick solid contours, interval $5 \cdot 10^{-5} \text{ s}^{-1}$ ) and the dilatation axes at 350 hPa in regions where $\Delta_m > 0$ (black arrows) at: (a) 00 UTC 26 Dec, (b) 12 UTC 26 Dec and (c) 00 UTC 27 Dec. . . . .	46
11	Time evolution of volume integrals over T1 (a) and T2 (b) between 250 and 900 hPa conditioned by $ \mathbf{F} \cdot \mathbf{B}_c  > 5 \cdot 10^{-4} \text{ m}^2 \cdot \text{s}^{-3}$ of the baroclinic potential energy generation rate $\mathbf{F} \cdot \mathbf{B}_c$ (thick solid line with diamonds), the low-frequency baroclinicity $ \mathbf{B}_c $ (dash-dotted line), the high-frequency total energy $T'_e$ (dotted line) and the exponential baroclinic generation rate term $\mathbf{F} \cdot \mathbf{B}_c / T'_e =  \mathbf{B}_c  \cdot \text{conf}$ (dashed line). Each integrated variable is divided by its maximum reached during the period considered in order to compare its evolution to other variables. 47	
12	Time evolution of the maximum of the vertically averaged high-frequency kinetic energy between 500 and 900 hPa around T1 (a) and T2 (b); time evolution of the maximum of the vertically averaged baroclinic conversion rate $-\mathcal{R}\theta'\omega'$ (dotted line with diamonds) and of the barotropic generation rate $\mathbf{E} \cdot \mathbf{D}_m$ (dotted line with stars) around T1 (c) and T2 (d). . . . .	48

- 13 Baroclinic configuration for T1 at 12 UTC 25 December (figs. a and c) and at 03 UTC 26 December (figs. b and d). In (a) and (b), high-frequency geopotential at 350 hPa (thick solid contours, interval  $500 \text{ m}^2\text{s}^{-2}$ ) and at 850 hPa (thick dashed contours, interval  $250 \text{ m}^2\text{s}^{-2}$ ) and vertically averaged (900-250 hPa) baroclinic potential energy generation rate  $\mathbf{F} \cdot \mathbf{B}_c$  (contour interval  $1.5 \cdot 10^{-3} \text{ m}^2 \cdot \text{s}^{-3}$ , light shadings with dashed contours and dark shadings with solid contours indicate respectively negative values smaller than  $-1.5 \cdot 10^{-3} \text{ m}^2 \cdot \text{s}^{-3}$  and positive values greater than  $1.5 \cdot 10^{-3} \text{ m}^2 \cdot \text{s}^{-3}$ ). The grey and black arrows represent respectively the baroclinicity vector  $\mathbf{B}_c$  and the high-frequency vector  $\mathbf{F}/T'_e$  both integrated vertically at the point where the vertical average of  $\mathbf{F} \cdot \mathbf{B}_c$  is maximum. In (c) and (d), vertical cross sections along  $\mathbf{F}$  of the high-frequency geopotential (thick dashed contours, interval  $250 \text{ m}^2\text{s}^{-2}$ ) and of  $\mathbf{F} \cdot \mathbf{B}_c$  (same definitions as in (a) and (b) but interval is  $3 \cdot 10^{-3} \text{ m}^2 \cdot \text{s}^{-3}$ ). . . . . 49
- 14 Baroclinic configuration for T2 at 00 UTC 27 December (figs. a and c) and at 15 UTC 27 December (figs. b and d). Same definitions of the contours as in Fig.13, but the only difference is the following; the contour interval for the vertical average of  $\mathbf{F} \cdot \mathbf{B}_c$  in (a) and (b) is  $3 \cdot 10^{-3} \text{ m}^2 \cdot \text{s}^{-3}$  and that for  $\mathbf{F} \cdot \mathbf{B}_c$  in (c) and (d) is  $6 \cdot 10^{-3} \text{ m}^2 \cdot \text{s}^{-3}$ . . . . . 50
- 15 Low-frequency wind speed  $|\mathbf{u}_m|$  at 850 hPa (dotted shadings and contour  $18 \text{ m} \cdot \text{s}^{-1}$ ), positive values of the low-frequency effective deformation  $\Delta_m$  at 850 hPa (shaded contours, interval  $2 \cdot 10^{-10} \text{ s}^{-2}$ ), high-frequency relative vorticity at 850 hPa larger than  $4 \cdot 10^{-5} \text{ s}^{-1}$  (thick solid contours, interval  $4 \cdot 10^{-5} \text{ s}^{-1}$ ), dilatation axes (black arrows) and stable axis (gray arrows) respectively defined by the angles  $0.5(\arccos(\pi/2 - 2\phi_m))$  and  $0.5(\arccos(-\frac{\zeta_m}{\sigma_m}) - 2\phi_m)$  with respect to the  $x$ -axis in regions where  $\Delta_m > 0$  ; (a) 12 UTC 25 Dec and (b) 12 UTC 26 Dec. . . . . 51

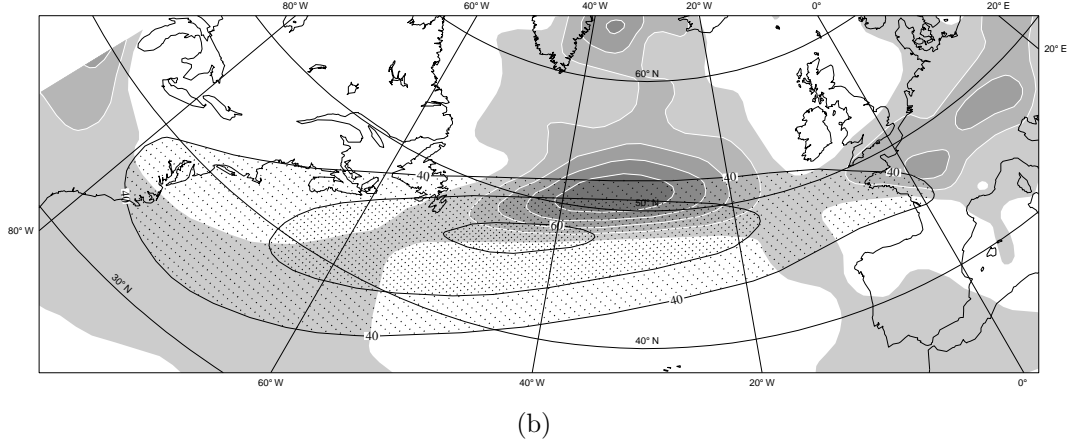
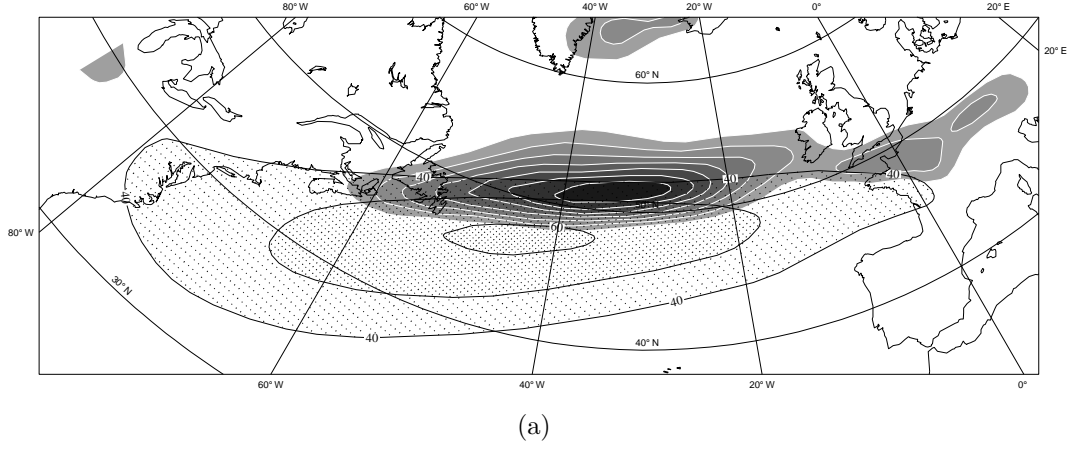
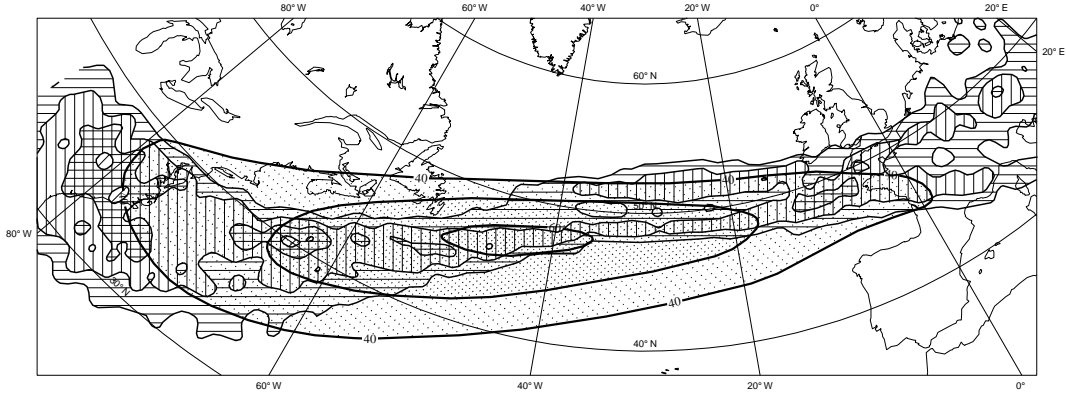
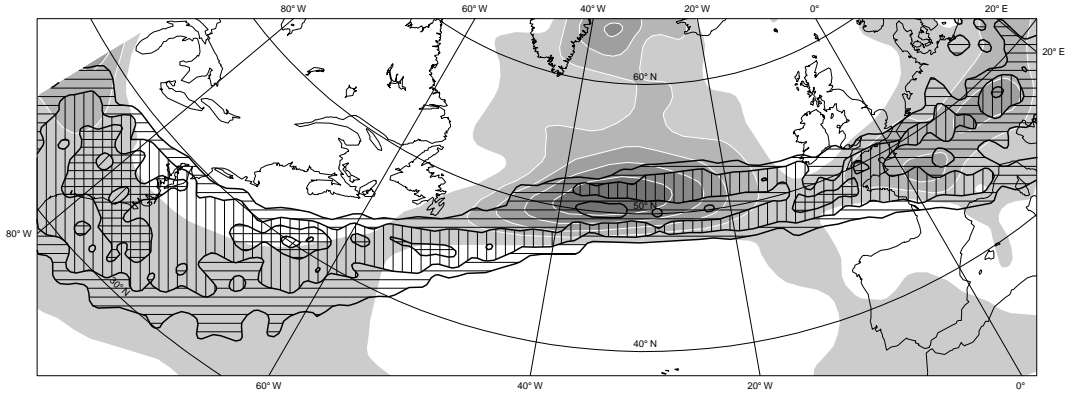


Figure 1: Low-frequency wind speed  $|\mathbf{u}_m|$  at 350 hPa larger than  $40 \text{ m.s}^{-1}$  (dotted shadings and contours, interval  $10 \text{ m.s}^{-1}$ ) with (a) the square of the low-frequency deformation vector modulus  $\sigma_m^2$  larger than  $9.10^{-10} \text{ s}^{-2}$  (shaded contours, interval  $9.10^{-10} \text{ s}^{-2}$ ) and (b) positive values of the low-frequency effective deformation  $\Delta_m$  (shaded contours, interval  $9.10^{-10} \text{ s}^{-2}$ ).

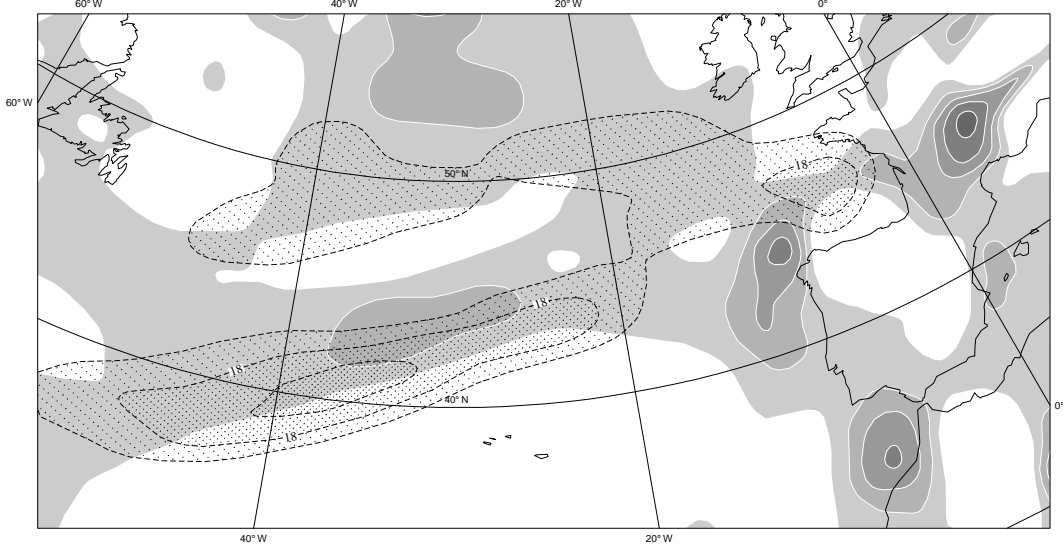


(a)

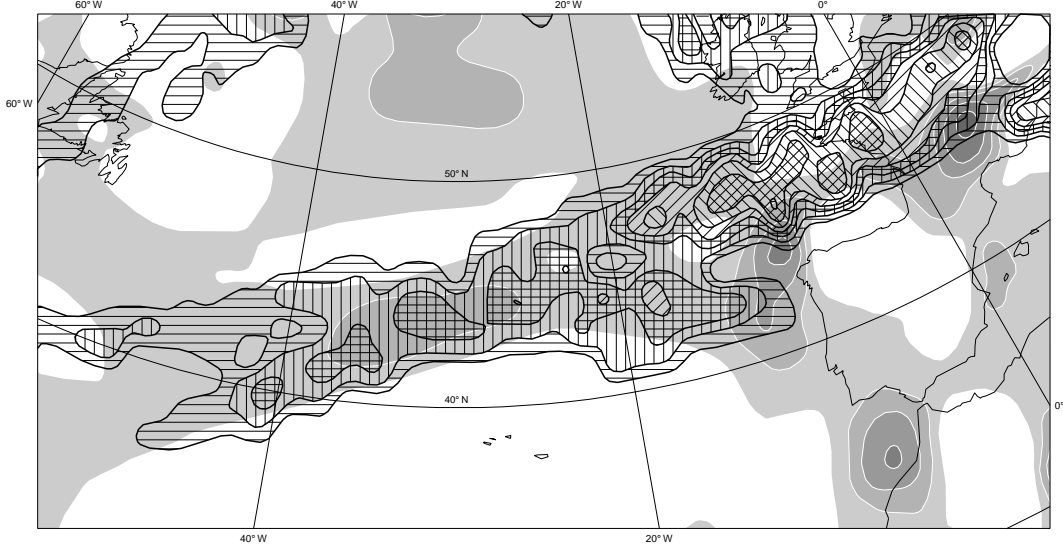


(b)

Figure 2: High-frequency relative vorticity density at 350 hPa during the period 23-28 December 1999 (number of times for which  $\zeta' > 1.25 \cdot 10^{-4} \text{ s}^{-1}$  at each grid point, hatched shadings) with (a) the low-frequency wind speed  $|\mathbf{u}_m|$  larger than  $40 \text{ m.s}^{-1}$  (dotted shadings and contours, interval  $10 \text{ m.s}^{-1}$ ) and (b) the positive values of the low-frequency effective deformation  $\Delta_m$  (shaded contours, interval  $9 \cdot 10^{-10} \text{ s}^{-2}$ ).

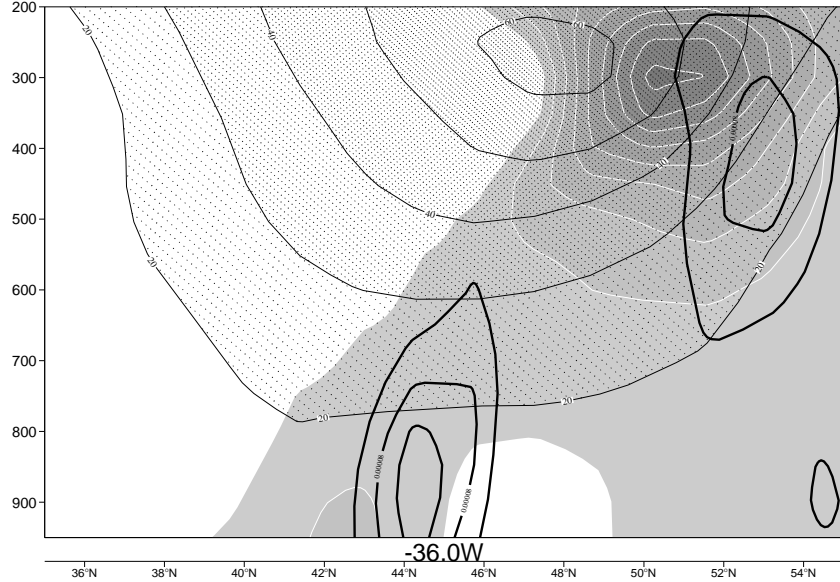


(a)

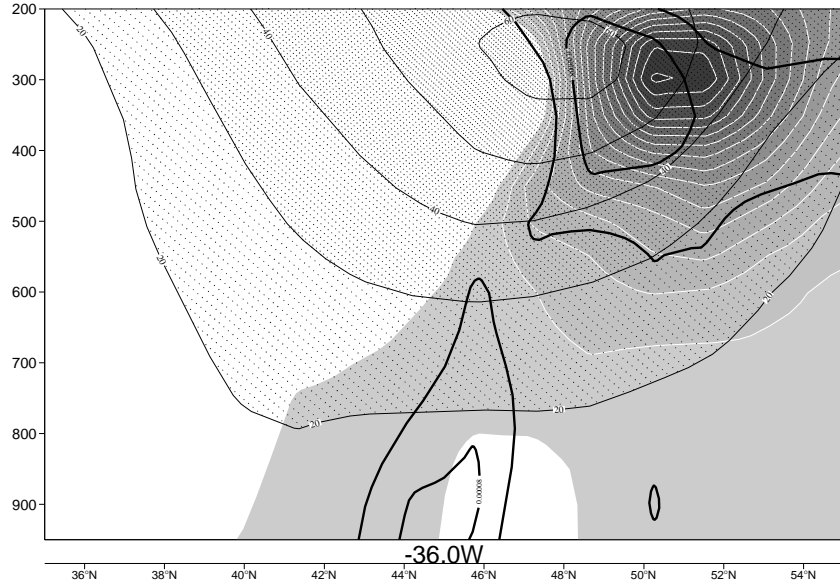


(b)

Figure 3: Positive values of the low-frequency effective deformation  $\Delta_m$  at 850 hPa (shaded contours, interval  $2 \cdot 10^{-10} \text{ s}^{-2}$ ) with (a) the low-frequency wind speed  $|\mathbf{u}_m|$  at 850 hPa (dotted shadings and dashed contours for 17, 18 and 19 m.s<sup>-1</sup>) and (b) high-frequency relative vorticity density at 850 hPa during the period 23-28 December 1999 (number of times for which  $\zeta' > 8 \cdot 10^{-5} \text{ s}^{-1}$  at each grid point, hatched shadings).



(a) 06 UTC 25 Dec



(b) 18 UTC 26 DEc

Figure 4: Vertical cross section of the low-frequency wind speed  $|\mathbf{u}_m|$  larger than  $20 \text{ m.s}^{-1}$  (dotted shadings and contours, interval  $10 \text{ m.s}^{-1}$ ), the positive values of  $\Delta_m$  (shaded contours, interval  $3 \cdot 10^{-10} \text{ s}^{-2}$ ) and the high-frequency relative vorticity larger than  $4 \cdot 10^{-5} \text{ s}^{-1}$  (thick solid contours, interval  $4 \cdot 10^{-5} \text{ s}^{-1}$ )

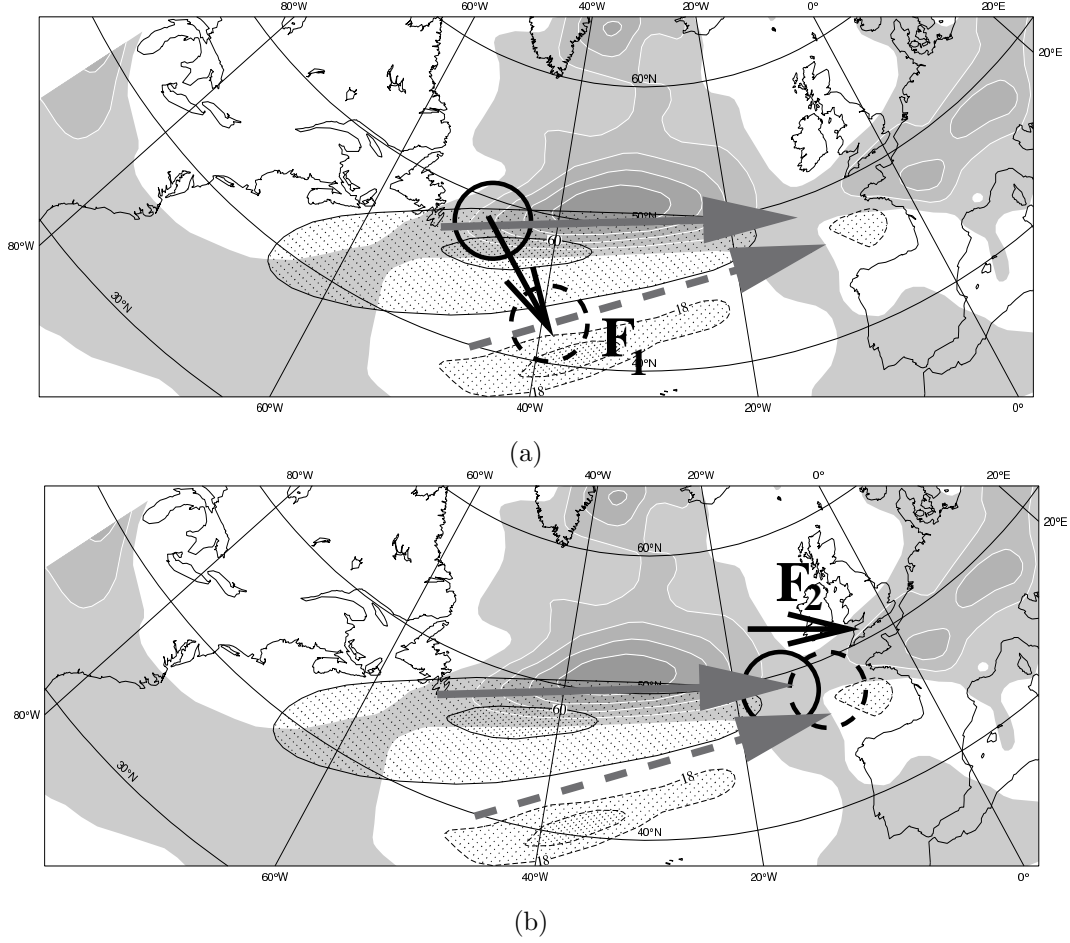
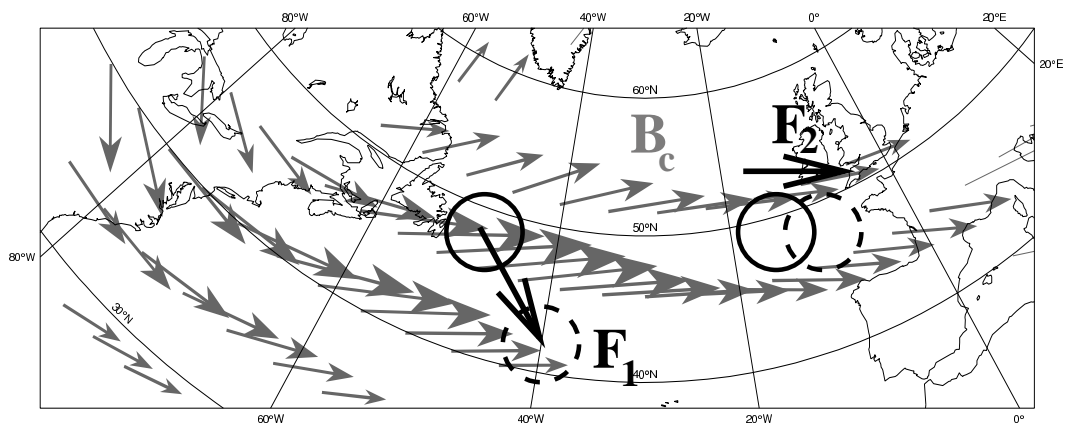


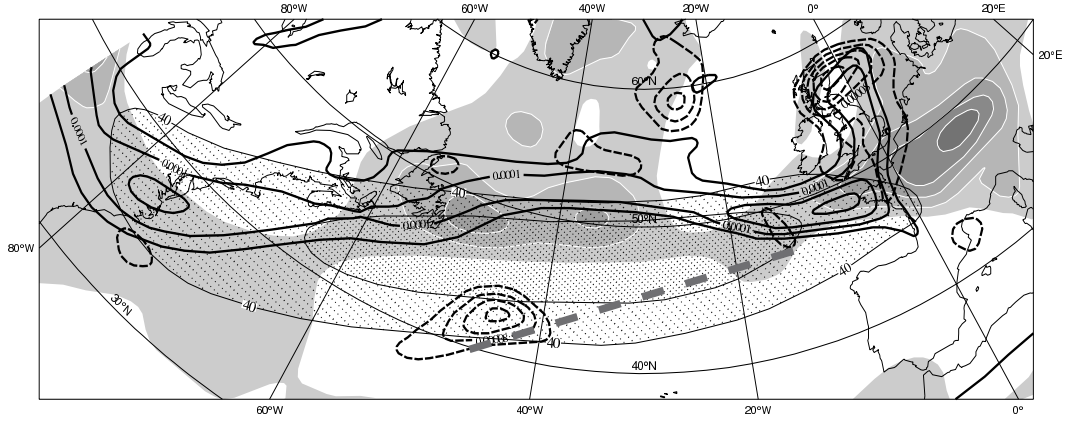
Figure 5: Schematic picture defining the baroclinic critical region. Low-frequency wind speed  $|\mathbf{u}_m|$  at 350 hPa larger than  $50 \text{ m.s}^{-1}$  (dotted shadings and solid contours, interval  $10 \text{ m.s}^{-1}$ ) and at 850 hPa (dotted shadings and dashed contours for 18 and  $19 \text{ m.s}^{-1}$ ). Positive values of the low-frequency effective deformation  $\Delta_m$  at 350 hPa are shown in shaded contours (interval  $9.10^{-10} \text{ s}^{-2}$ ). The solid and dashed gray arrows represent respectively regions with positive values of  $\Delta_m$  at 350 hPa and 850 hPa from the jet core to its exit which are both located on the northern side of their respective jets. The convergence of these two arrows in the jet-exit region defines the baroclinic critical region. The solid and dashed black circles represent respectively high-frequency disturbances at 350 hPa and 850 hPa evolving (a) in the jet-core region and (b) in the jet-exit region. The black arrows denoted  $\mathbf{F}_1$  and  $\mathbf{F}_2$  are the  $\mathbf{F}$  vector for two different configuration cases shown respectively in (a) and (b). In (c),  $\mathbf{F}_1$  and  $\mathbf{F}_2$  are superposed to the vertically averaged (900-250hPa) baroclinicity vector  $\mathbf{B}_c$  when  $|\mathbf{B}_c| > 2.10^{-5} \text{ s}^{-1}$ .



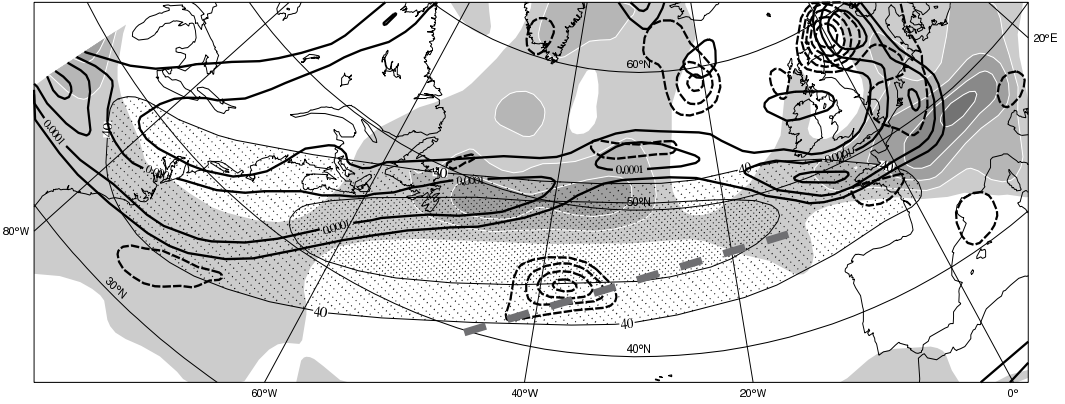


(c)

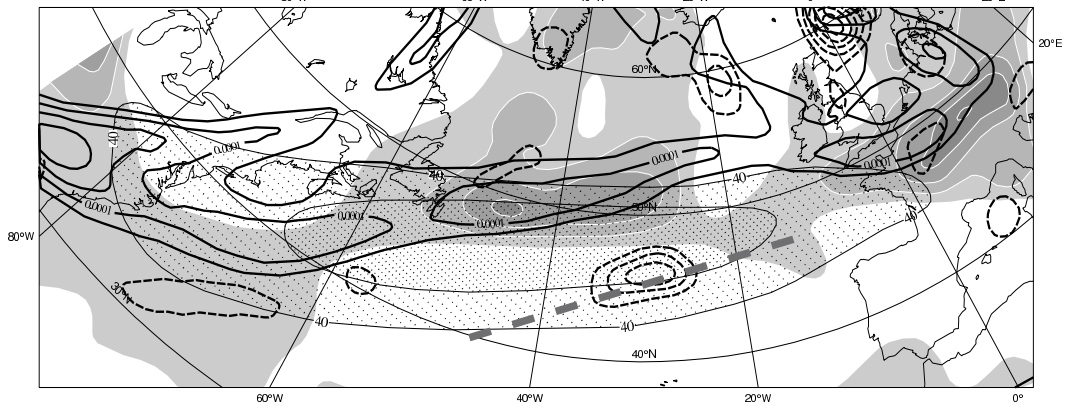
Figure 5. (Continued)



(a) 00 UTC 25 Dec

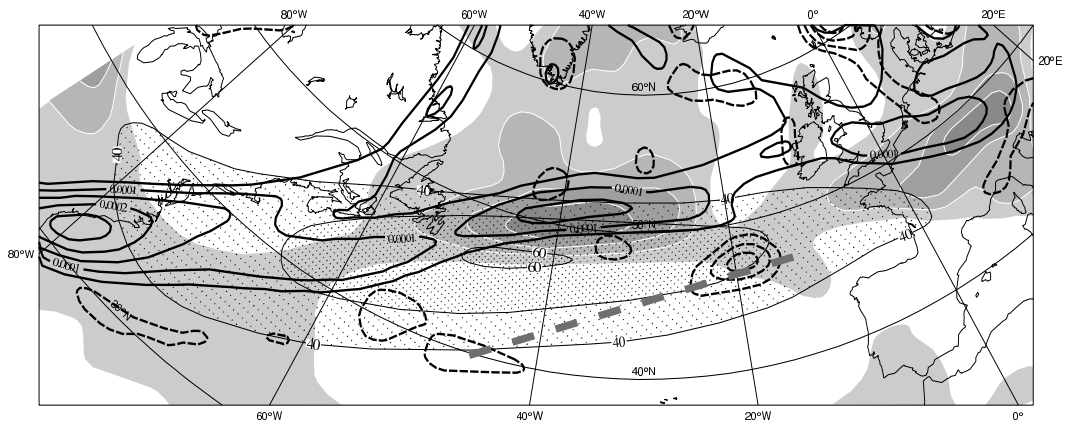


(b) 06 UTC 25 Dec

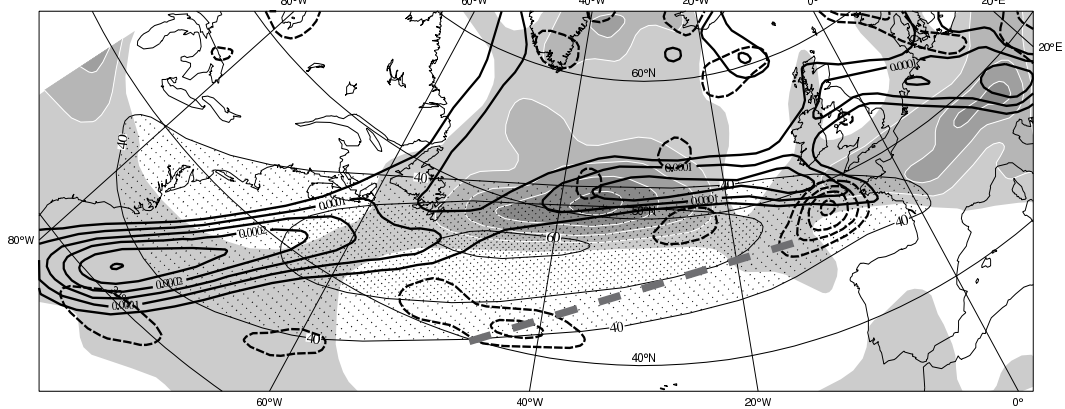


(c) 12 UTC 25 Dec

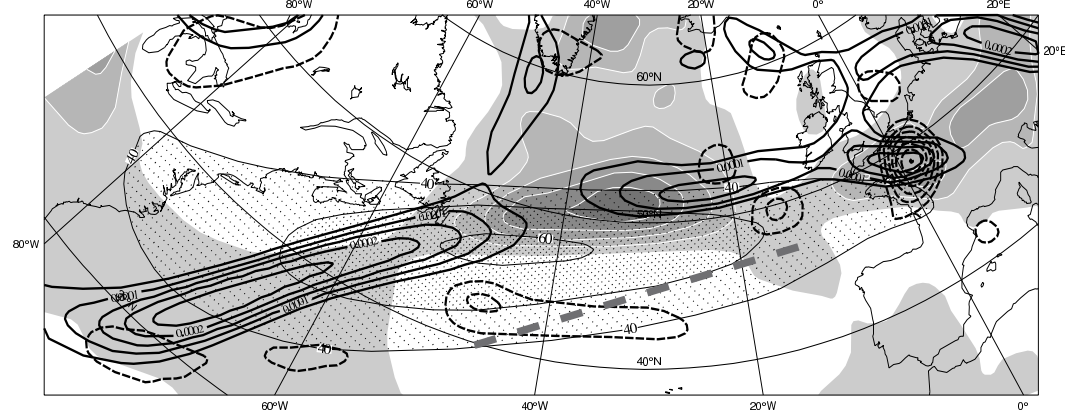
Figure 6: Low-frequency wind speed  $|\mathbf{u}_m|$  at 350 hPa larger than  $40 \text{ m.s}^{-1}$  (dotted shadings and contours, interval  $10 \text{ m.s}^{-1}$ ), positive values of the low-frequency effective deformation  $\Delta_m$  at 350 hPa (shaded contours, interval  $9 \cdot 10^{-10} \text{ s}^{-2}$ ), high-frequency relative vorticity at 350 hPa larger than  $5 \cdot 10^{-5} \text{ s}^{-1}$  (thick solid contours, interval  $5 \cdot 10^{-5} \text{ s}^{-1}$ ) and high-frequency relative vorticity at 850 hPa larger than  $4 \cdot 10^{-5} \text{ s}^{-1}$  (thick dashed contours, interval  $4 \cdot 10^{-5} \text{ s}^{-1}$ ): (a) 00 UTC 25 Dec, (b) 06 UTC 25 Dec, and (c) 12 UTC 25 Dec. The dashed gray line corresponds to the same axis as the dashed gray arrow of Fig.5, i.e to the thin region of positive  $\Delta_m$  at 850 hPa.



(a) 18 UTC 25 Dec

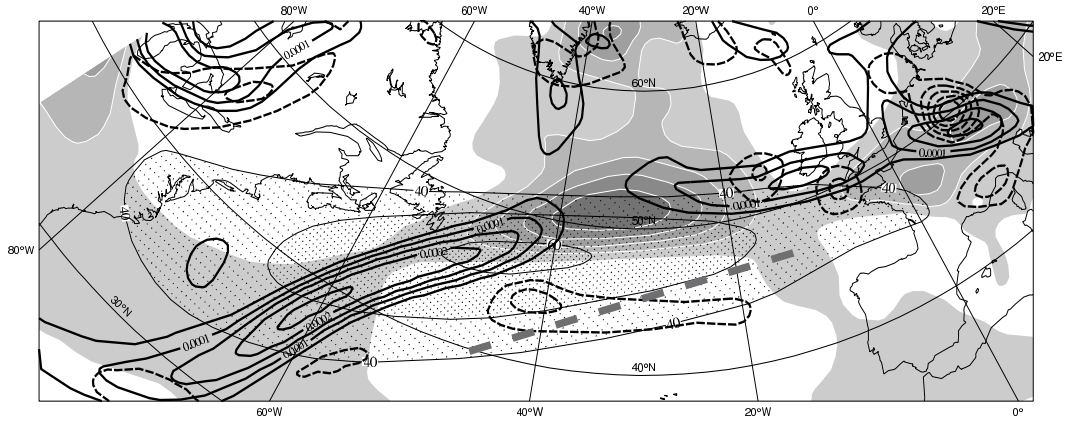


(b) 00 UTC 26 Dec

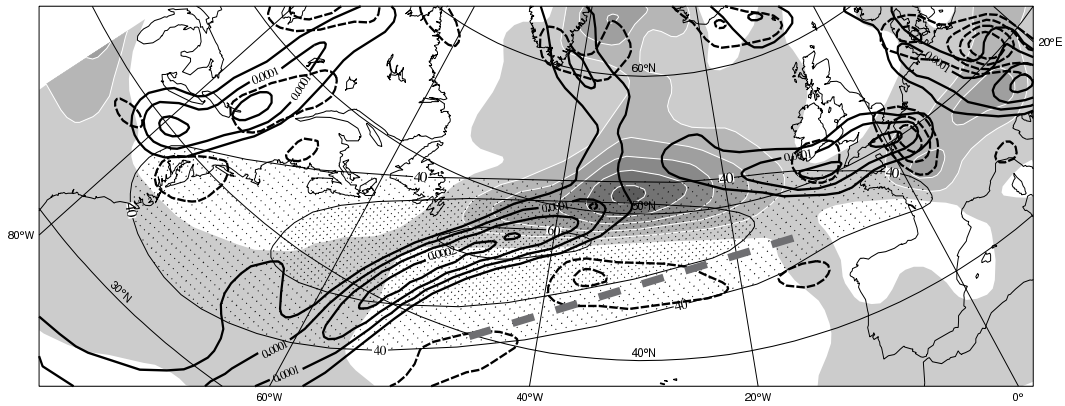


(c) 06 UTC 26 Dec

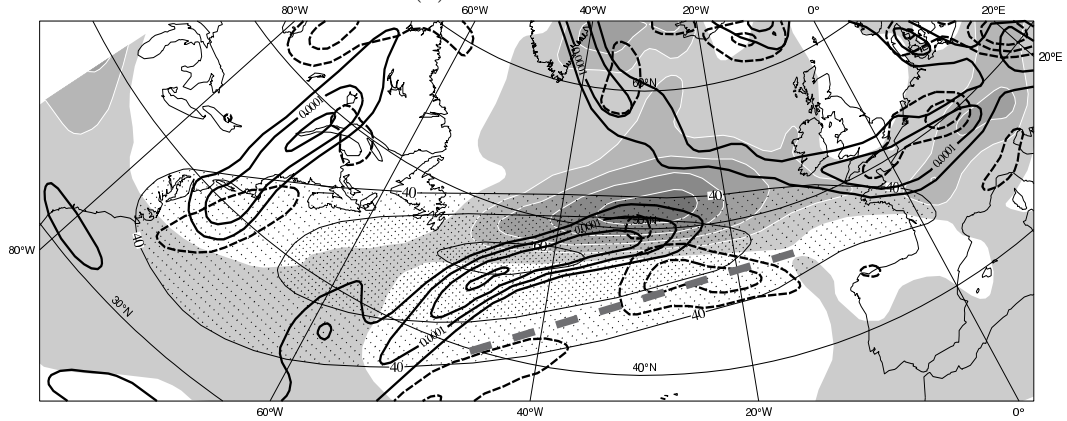
Figure 7: Same as in Fig.6, but for (a) 18 UTC 25 Dec, (b) 00 UTC 26 Dec and (c) 06 UTC 26 Dec.



(a) 12 UTC 26 Dec



(b) 18 UTC 26 Dec



(c) 00 UTC 27 Dec

Figure 8: Same as in Fig.6, but for (a) 12 UTC 26 Dec, (b) 18 UTC 26 Dec and (c) 00 UTC 27 Dec.

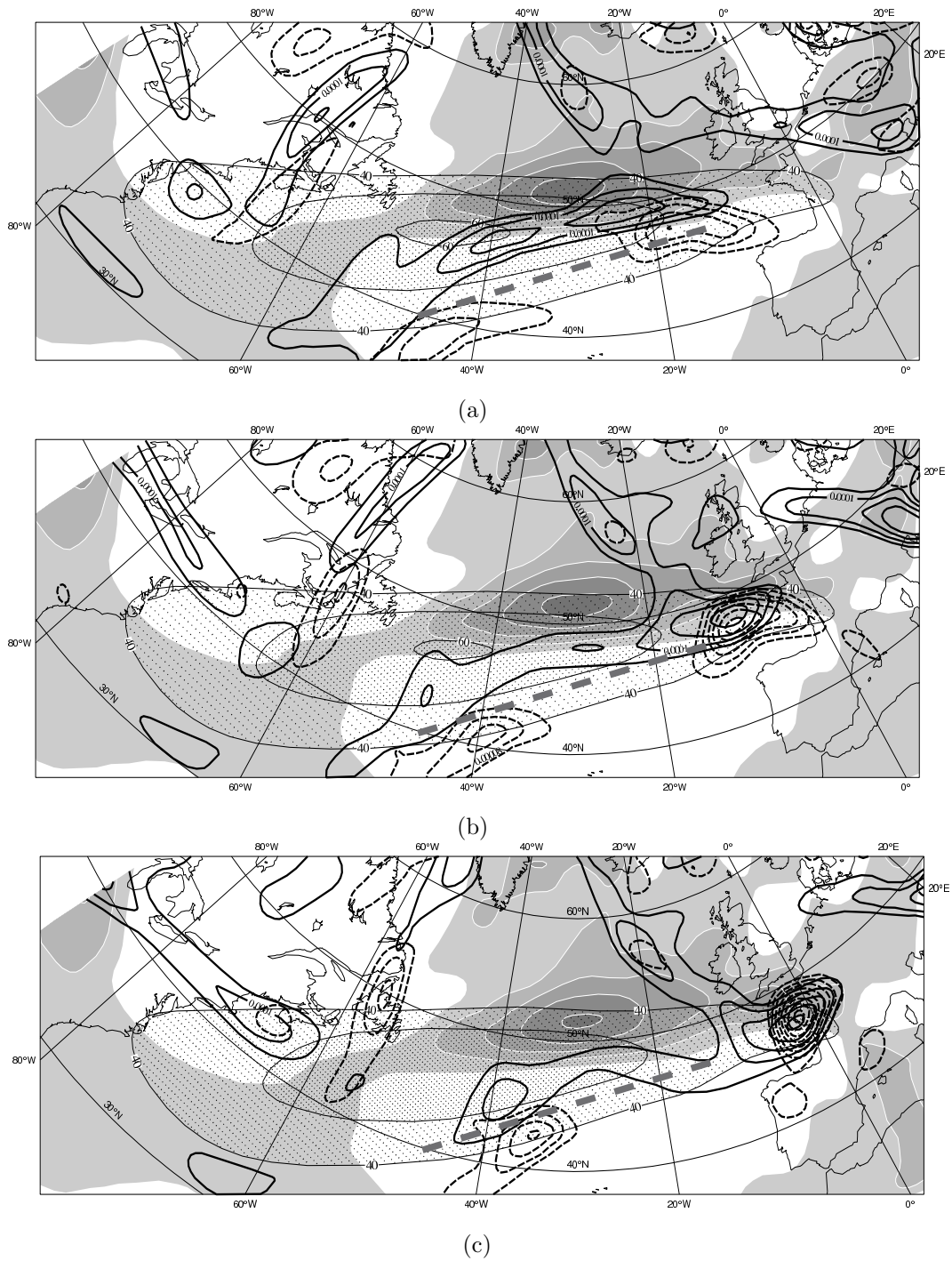
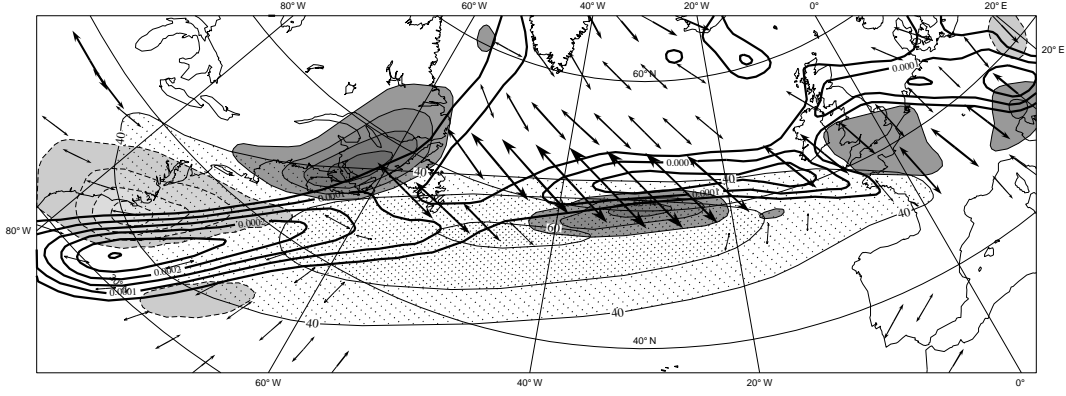
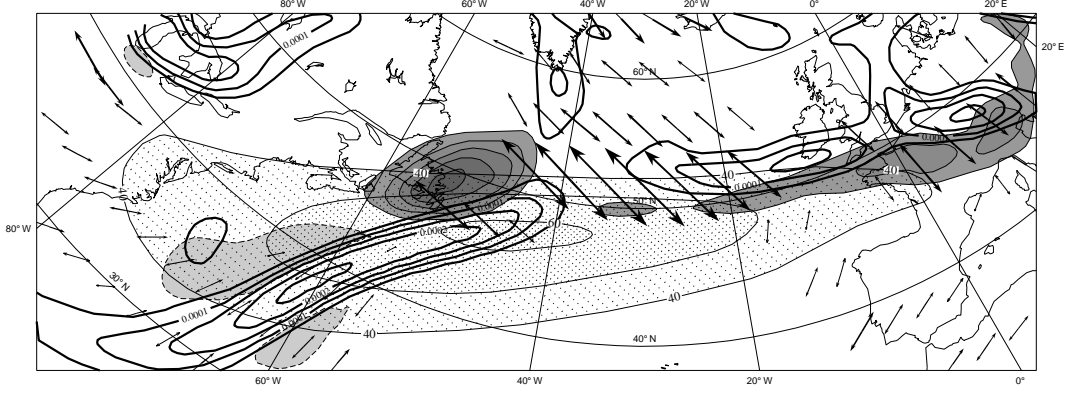


Figure 9: Same as in Fig.6, but for (a) 06 UTC 27 Dec, (b) 12 UTC 27 Dec and (c) 18 UTC 27 Dec.

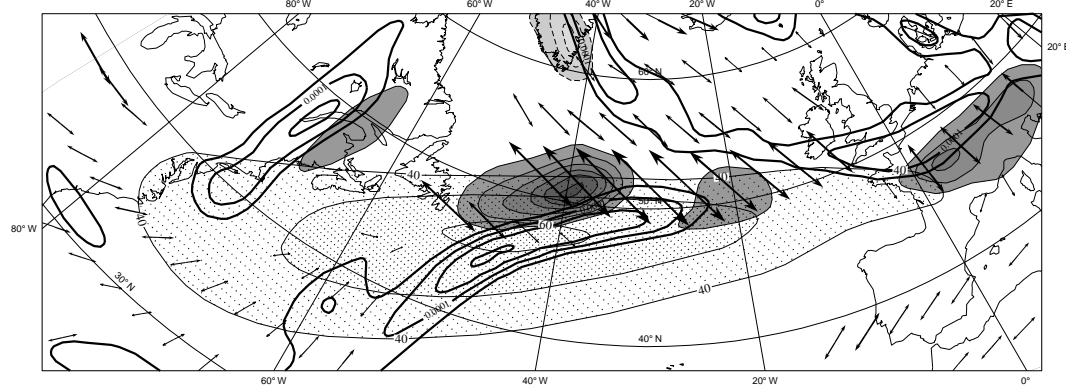




(a) 00 UTC 26 Dec

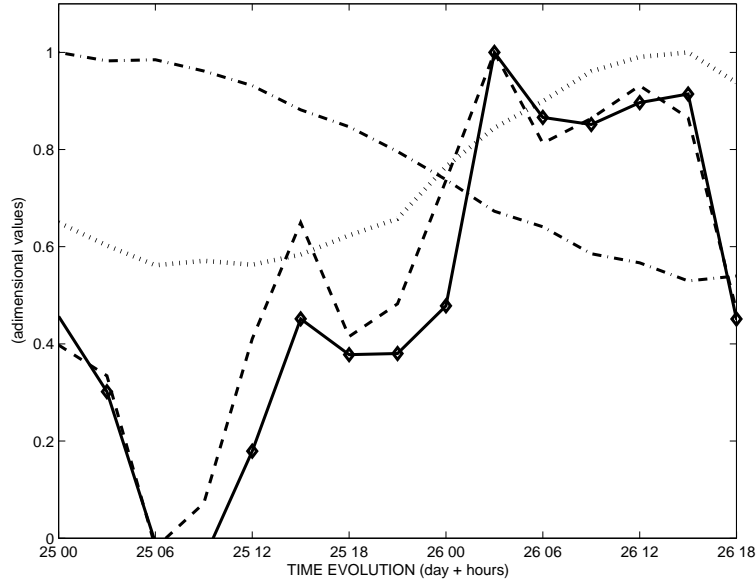


(b) 12 UTC 26 Dec

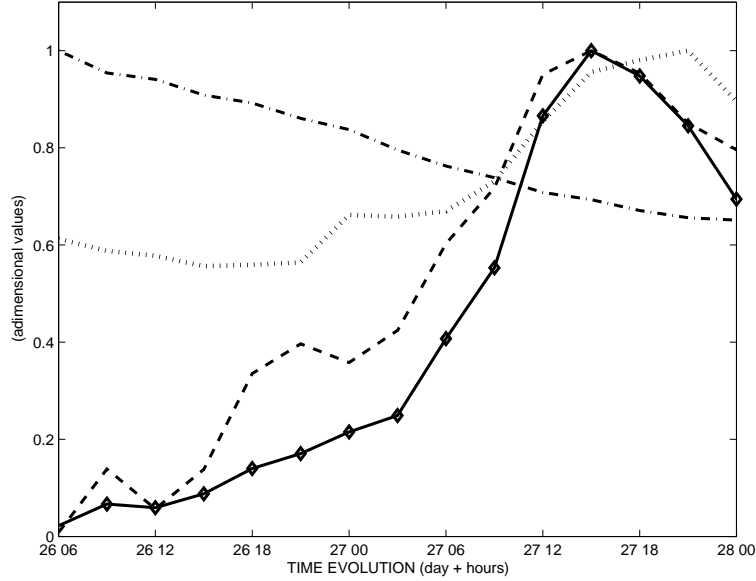


(c) 00 UTC 27 Dec

Figure 10: Barotropic generation rate  $\mathbf{E} \cdot \mathbf{D}_m$  at 350 hPa (contour interval is  $0.01 \text{ m}^2 \cdot \text{s}^{-3}$ , light shadings with dashed contours and dark shadings with solid contours indicate respectively negative values smaller than  $-0.01 \text{ m}^2 \cdot \text{s}^{-3}$  and positive values greater than  $0.01 \text{ m}^2 \cdot \text{s}^{-3}$ ), low-frequency wind speed  $|\mathbf{u}_m|$  at 350 hPa larger than  $40 \text{ m} \cdot \text{s}^{-1}$  (dotted shadings), the high-frequency relative vorticity larger than  $5 \cdot 10^{-5} \text{ s}^{-1}$  (thick solid contours, interval  $5 \cdot 10^{-5} \text{ s}^{-1}$ ) and the dilatation axes at 350 hPa in regions where  $\Delta_m > 0$  (black arrows) at: (a) 00 UTC 26 Dec, (b) 12 UTC 26 Dec and (c) 00 UTC 27 Dec.



(a)



(b)

Figure 11: Time evolution of volume integrals over T1 (a) and T2 (b) between 250 and 900 hPa conditioned by  $|\mathbf{F} \cdot \mathbf{B}_c| > 5 \cdot 10^{-4} \text{ m}^2 \cdot \text{s}^{-3}$  of the baroclinic potential energy generation rate  $\mathbf{F} \cdot \mathbf{B}_c$  (thick solid line with diamonds), the low-frequency baroclinicity  $|\mathbf{B}_c|$  (dash-dotted line), the high-frequency total energy  $T'_e$  (dotted line) and the exponential baroclinic generation rate term  $\mathbf{F} \cdot \mathbf{B}_c / T'_e = |\mathbf{B}_c| \cdot \text{conf}$  (dashed line). Each integrated variable is divided by its maximum reached during the period considered in order to compare its evolution to other variables.

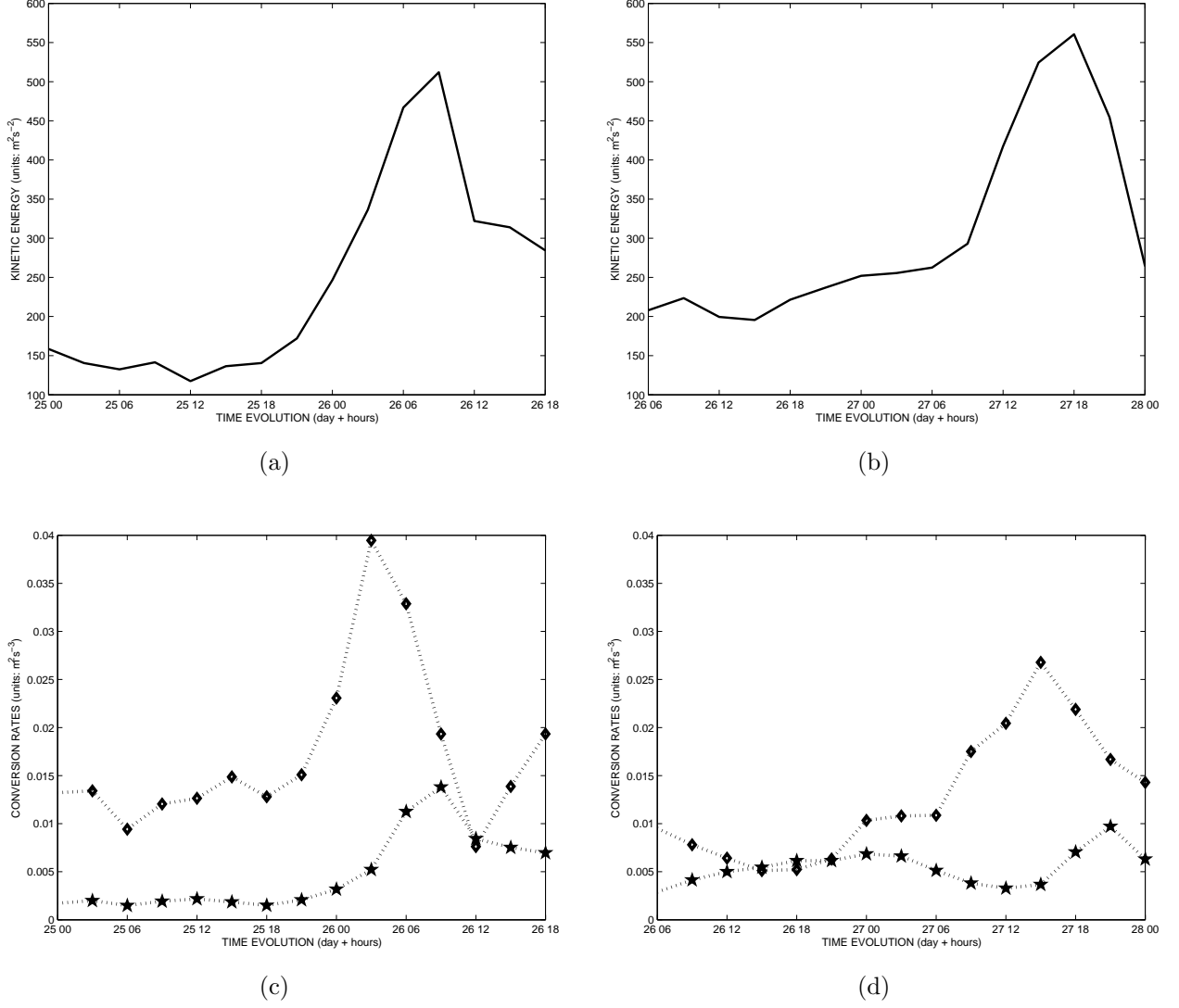
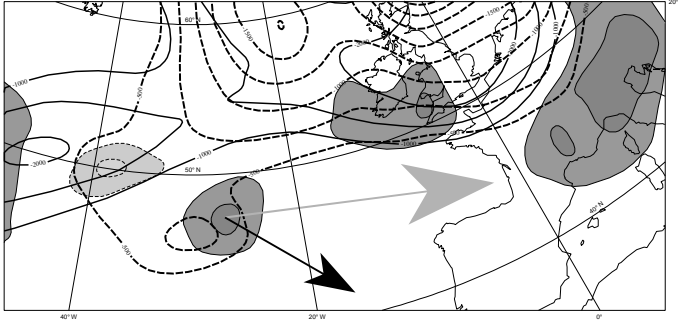
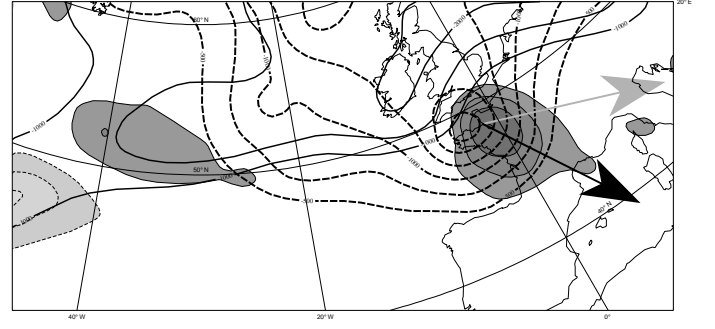


Figure 12: Time evolution of the maximum of the vertically averaged high-frequency kinetic energy between 500 and 900 hPa around T1 (a) and T2 (b); time evolution of the maximum of the vertically averaged baroclinic conversion rate  $-\mathcal{R}\theta'\omega'$  (dotted line with diamonds) and of the barotropic generation rate  $\mathbf{E} \cdot \mathbf{D}_m$  (dotted line with stars) around T1 (c) and T2 (d).

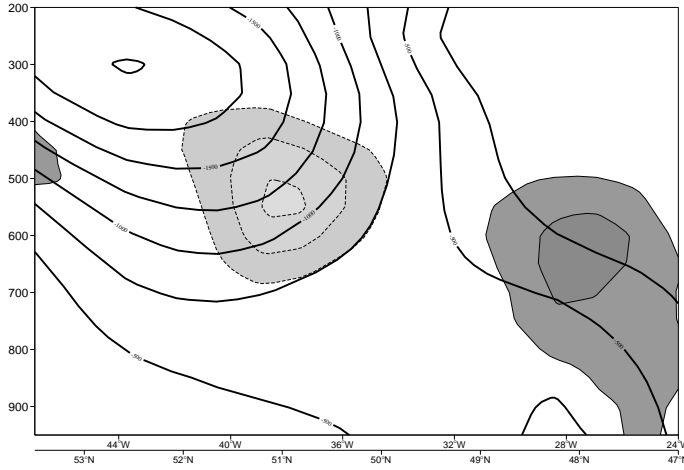




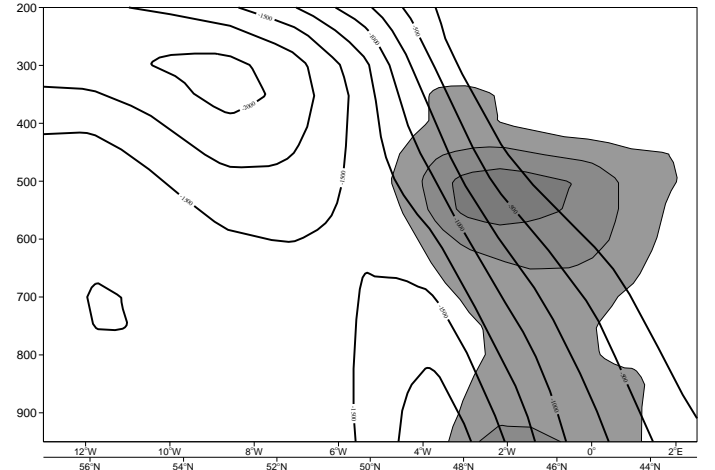
(a)  $\mathbf{F} \cdot \mathbf{B}_c$ , HF geopotential, 12 UTC 25 Dec.



(b)  $\mathbf{F} \cdot \mathbf{B}_c$ , HF geopotential, 03 UTC 26 Dec.

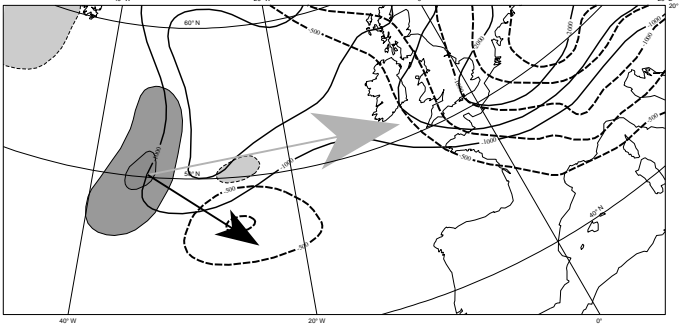


(c) Cross section along  $\mathbf{F}$ ,  $\mathbf{F} \cdot \mathbf{B}_c$ , 12 UTC 25 Dec.

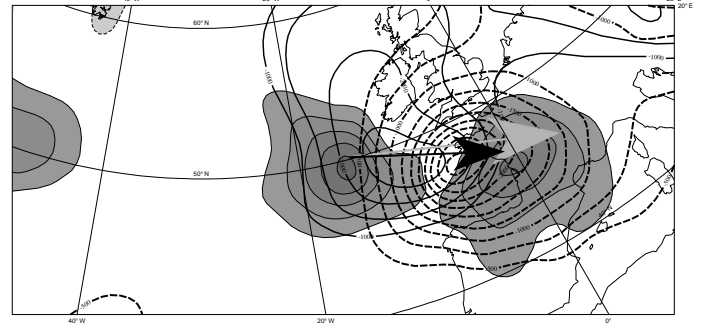


(d) Cross section along  $\mathbf{F}$ ,  $\mathbf{F} \cdot \mathbf{B}_c$ , 03 UTC 26 Dec.

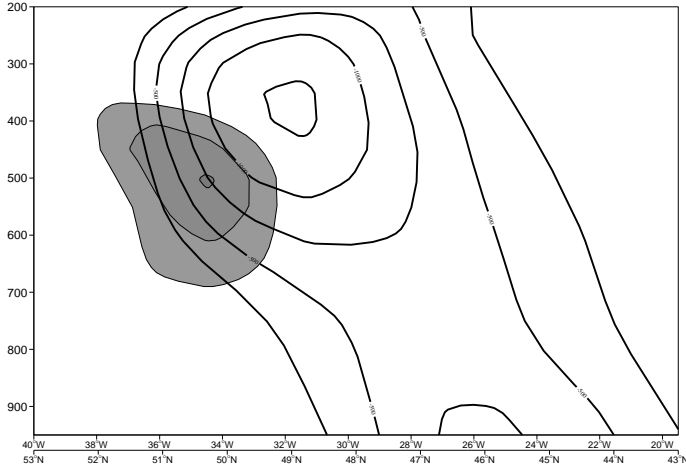
Figure 13: Baroclinic configuration for T1 at 12 UTC 25 December (figs. a and c) and at 03 UTC 26 December (figs. b and d). In (a) and (b), high-frequency geopotential at 350 hPa (thick solid contours, interval  $500 \text{ m}^2\text{s}^{-2}$ ) and at 850 hPa (thick dashed contours, interval  $250 \text{ m}^2\text{s}^{-2}$ ) and vertically averaged (900-250 hPa) baroclinic potential energy generation rate  $\mathbf{F} \cdot \mathbf{B}_c$  (contour interval  $1.5 \cdot 10^{-3} \text{ m}^2\text{s}^{-3}$ , light shadings with dashed contours and dark shadings with solid contours indicate respectively negative values smaller than  $-1.5 \cdot 10^{-3} \text{ m}^2\text{s}^{-3}$  and positive values greater than  $1.5 \cdot 10^{-3} \text{ m}^2\text{s}^{-3}$ ). The grey and black arrows represent respectively the baroclinicity vector  $\mathbf{B}_c$  and the high-frequency vector  $\mathbf{F}/T'_e$  both integrated vertically at the point where the vertical average of  $\mathbf{F} \cdot \mathbf{B}_c$  is maximum. In (c) and (d), vertical cross sections along  $\mathbf{F}$  of the high-frequency geopotential (thick dashed contours, interval  $250 \text{ m}^2\text{s}^{-2}$ ) and of  $\mathbf{F} \cdot \mathbf{B}_c$  (same definitions as in (a) and (b) but interval is  $3 \cdot 10^{-3} \text{ m}^2\text{s}^{-3}$ ).



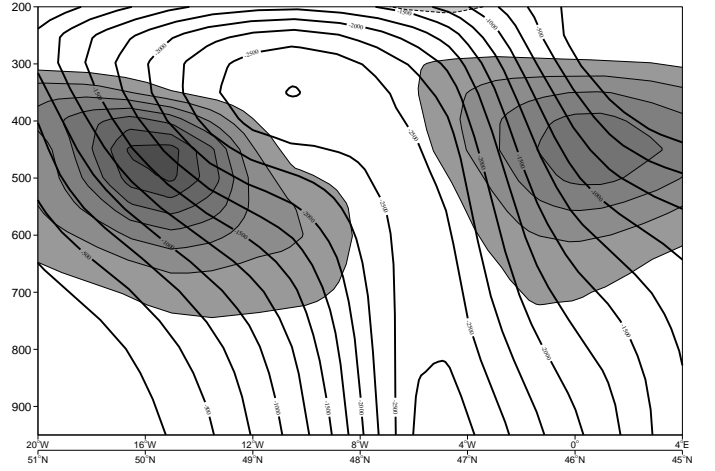
(a)  $\mathbf{F} \cdot \mathbf{B}_c$ , HF geopotential, 00 UTC 27 Dec.



(b)  $\mathbf{F} \cdot \mathbf{B}_c$ , HF geopotential, 15 UTC 27 Dec.

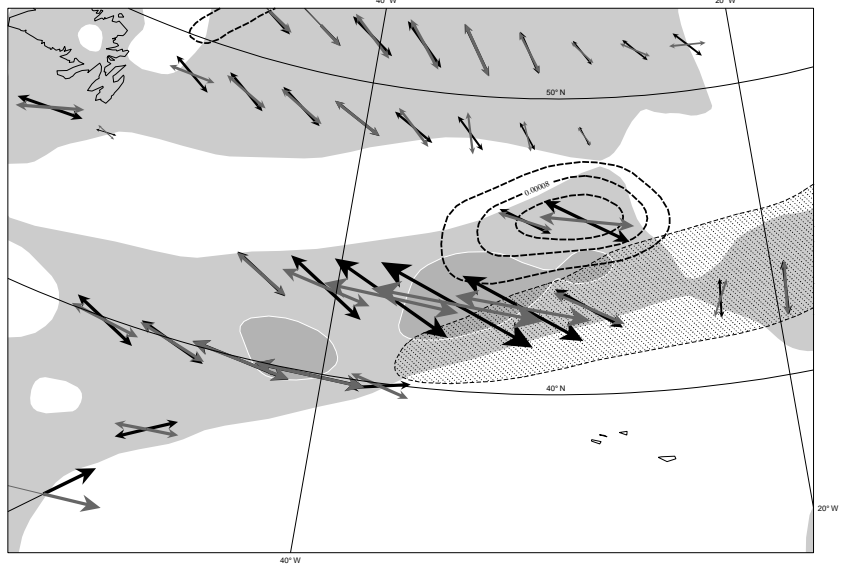


(c) Cross section along  $\mathbf{F}$ ,  $\mathbf{F} \cdot \mathbf{B}_c$ , 00 UTC 27 Dec.

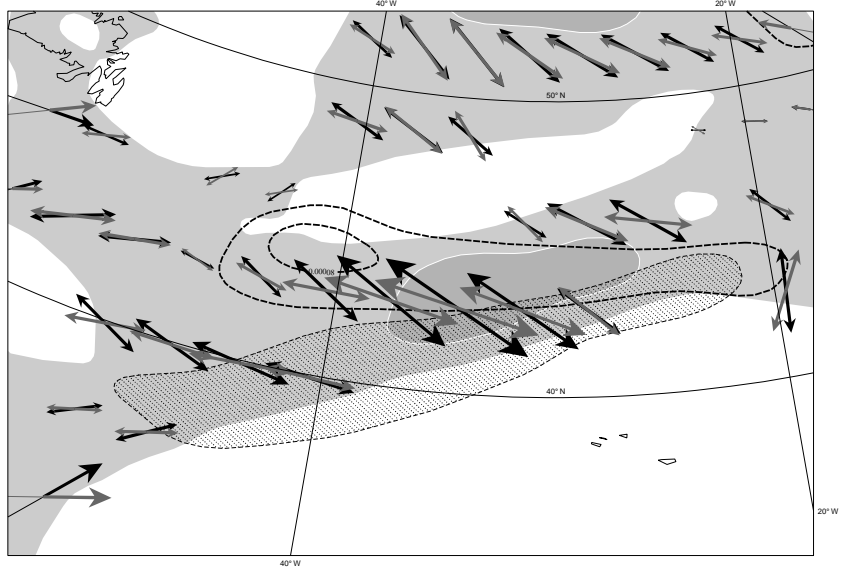


(d) Cross section along  $\mathbf{F}$ ,  $\mathbf{F} \cdot \mathbf{B}_c$ , 15 UTC 27 Dec.

Figure 14: Baroclinic configuration for T2 at 00 UTC 27 December (figs. a and c) and at 15 UTC 27 December (figs. b and d). Same definitions of the contours as in Fig.13, but the only difference is the following; the contour interval for the vertical average of  $\mathbf{F} \cdot \mathbf{B}_c$  in (a) and (b) is  $3 \cdot 10^{-3} \text{ m}^2 \cdot \text{s}^{-3}$  and that for  $\mathbf{F} \cdot \mathbf{B}_c$  in (c) and (d) is  $6 \cdot 10^{-3} \text{ m}^2 \cdot \text{s}^{-3}$ .



(a)



(b)

Figure 15: Low-frequency wind speed  $|\mathbf{u}_m|$  at 850 hPa (dotted shadings and contour  $18 \text{ m.s}^{-1}$ ), positive values of the low-frequency effective deformation  $\Delta_m$  at 850 hPa (shaded contours, interval  $2 \cdot 10^{-10} \text{ s}^{-2}$ ), high-frequency relative vorticity at 850 hPa larger than  $4 \cdot 10^{-5} \text{ s}^{-1}$  (thick solid contours, interval  $4 \cdot 10^{-5} \text{ s}^{-1}$ ), dilatation axes (black arrows) and stable axis (gray arrows) respectively defined by the angles  $0.5(\arccos(\pi/2 - 2\phi_m))$  and  $0.5(\arccos(-\frac{\zeta_m}{\sigma_m}) - 2\phi_m)$  with respect to the  $x$ -axis in regions where  $\Delta_m > 0$  ; (a) 12 UTC 25 Dec and (b) 12 UTC 26 Dec.